Click here to view PowerPoint presentation; Press Esc to exit

VLF Phase Perturbations Produced by the Variability in Large (V/m) Mesospheric Electric Fields in the 60 – 70 km Altitude Range

A.H. Manson, C.E. Meek
Institute Space & Atmospheric Studies
University of Saskatchewan
116 Science Place
Saskatoon, SK S7N 5E2
CANADA

ahm373@mail.usask.ca / meek@dansas.usask.ca

S.I. Martynenko, V.T. Rozumenko, O.F. Tyrnov
Department of Space Radio Physics
School of Radio Physics
Kharkiv V. Karazin National University
4 Svoboda Square, Kharkiv 61077
UKRAINE

Sergey.I.Martynenko@univer.kharkov.ua / Victor.T.Rozumenko@univer.kharkov.ua /
Oleg.F.Tyrnov@univer.kharkov.ua

ABSTRACT

The large (V/m) mesospheric electric fields have been identified as a possible cause of VLF phase perturbations. These fields affect the fundamental processes that govern the lower D region parameters, primarily the electron temperature and effective collision frequency. The main ionospheric parameter needed to calculate VLF phase perturbations is the low-frequency electron plasma conductivity. All the electric field data available to 1990 were collected with electric field sensors on board more than 50 rockets launched over approximately 30 years in the USSR and the U.S.A., which were insufficient to address VLF phase perturbations. This paper discusses the progress made in addressing large (V/m) mesospheric electric fields between 60- and 70-km altitudes since 1990. It focuses on achieving the breakthrough, the development of a radio wave technique for sensing large electric fields remotely by using MF radar, and on the fact that the electric field variability leads to the variability of ionospheric conduction contours by a few kilometers in altitude. The statistical analysis of the large mesospheric electric field data acquired in the 60- and 67-km altitude region in Canada and Ukraine suggests that large mesospheric electric fields may occur during about 70% of all the time. However, reasonable assessments of VLF phase perturbations need information on the temporal and especially spatial variability of conduction contours, which remains a major challenge within this problem. First, the technique developed to specify electric fields requires signal-to-noise ratios in excess of a factor of five, which is achieved irregularly with the MF radars used at present. Second, the existing MF radars do not permit the observations of the spatial evolution of these fields at all. The latter problem can be overcome by developing dedicated radar. Meanwhile, co-located VLF phase perturbation measurements and electric field observations by existing MF radars may be combined to produce a pre-intermediate capability. Eventually, a better understanding of the dynamics and mesospheric and ionospheric D-region chemistry, which establish conductivity patterns, will require the combined efforts of the entire scientific community.

Manson, A.H.; Meek, C.E.; Martynenko, S.I.; Rozumenko, V.T.; Tyrnov, O.F. (2006) VLF Phase Perturbations Produced by the Variability in Large (V/m) Mesospheric Electric Fields in the 60 – 70 km Altitude Range. In *Characterising the Ionosphere* (pp. 8-1 – 8-24). Meeting Proceedings RTO-MP-IST-056, Paper 8. Neuilly-sur-Seine, France: RTO. Available from: http://www.rto.nato.int/abstracts.asp.

Report Documentation Page

Form Approved
OMB No. 0704-0188

1. REPORT DATE	2. REPORT TYPE	3. DATES COVERED
01 JUN 2006	**N/A**	**-**

4. TITLE AND SUBTITLE	5a. CONTRACT NUMBER
VLF Phase Perturbations Produced by the Variability in Large (V/m) Mesospheric Electric Fields in the 60 70 km Altitude Range	5b. GRANT NUMBER
	5c. PROGRAM ELEMENT NUMBER
6. AUTHOR(S)	5d. PROJECT NUMBER
	5e. TASK NUMBER
	5f. WORK UNIT NUMBER
7. PERFORMING ORGANIZATION NAME(S) AND ADDRESS(ES) **Institute Space & Atmospheric Studies University of Saskatchewan 116 Science Place Saskatoon, SK S7N 5E2 CANADA**	8. PERFORMING ORGANIZATION REPORT NUMBER
9. SPONSORING/MONITORING AGENCY NAME(S) AND ADDRESS(ES)	10. SPONSOR/MONITOR'S ACRONYM(S)
	11. SPONSOR/MONITOR'S REPORT NUMBER(S)

12. DISTRIBUTION/AVAILABILITY STATEMENT
Approved for public release, distribution unlimited

13. SUPPLEMENTARY NOTES
See also ADM002065., The original document contains color images.

14. ABSTRACT

15. SUBJECT TERMS

16. SECURITY CLASSIFICATION OF:			17. LIMITATION OF ABSTRACT	18. NUMBER OF PAGES	19a. NAME OF RESPONSIBLE PERSON
a. REPORT	b. ABSTRACT	c. THIS PAGE			
unclassified	**unclassified**	**unclassified**	**UU**	**59**	

1.0 INTRODUCTION

The mesosphere is an active electrodynamic region where large volt/meter mesospheric electric fields are generated locally. Much of the evidence for and against large mesospheric electric fields exist to 1990 is collected in the reviews by *Goldberg* [1 – 3]. All the data to 1990 were obtained with electric field sensors on board more than 50 rockets launched over about 30 years in the USSR and the U.S.A., and they were reported in tens of research papers [e.g., 1– 4, 33 and references cited therein].

Figure 1, taken from the paper by *Maynard et al*. [4]), shows representative vertical electric field profiles from rocket-borne probes. The large mesospheric electric fields usually occur in a layer of order 10 km thick above about 60 km.

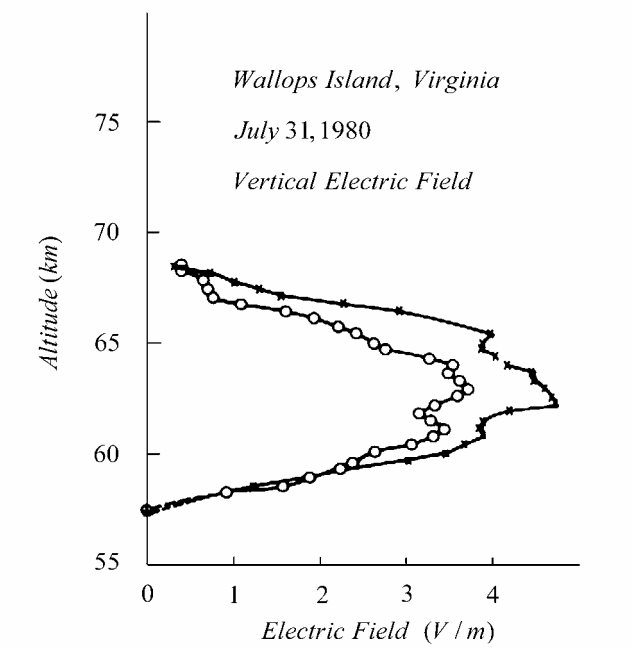

Figure 1. Electric field profiles from rocket-borne symmetric double probes at Wallops Island, Virginia, on 31 July 1980 (after Maynard et al. [4]). The two profiles represent *x* and *y* axis sensors, which were prepared with different coatings.

The possible physical mechanisms responsible for the generation of large mesospheric electric fields have been developed in a few papers [5 – 8]. These theoretical models provide the main conditions for the occurrence of apparent V/m electric fields in the lower mesosphere, winds and heavy ions.

Seen from our state of knowledge in 1990, a remote sensing instrument employing a radio-wave technique was critical to achieving the scientific breakthrough necessary to investigate the electrodynamics of the mesosphere.

Since 1990, we have developed a radio wave technique for remotely sensing large volt/meter electric fields, which are intrinsic to the mesosphere [9 – 14].

Over the years, the MF radars in Canada and Ukraine have accumulated a dataset of about 350 separate 5 – 10 min intervals of measurements, which is greater then the entire rocket dataset of these fields. The MF radar dataset has yielded knowledge on the local height and temporal evolution of these fields. However, this dataset does not contain at all information about the three-dimensional distribution of mesospheric electric fields, and therefore it is insufficient to model VLF phase perturbations thoroughly. The determination of the electric field spatial distribution poses a major challenge for the future.

The next section will present the MF radar technique for determining large mesospheric electric fields and the summary of its capabilities. Section 3 will describe the disturbances in conductivity profiles, which emerge from modeling studies. Section 4 will state the challenges in determining VLF phase perturbations produced by large mesospheric electric fields. Section 5 will indicate the immediate benefits of co-located VLF phase perturbation measurements and electric field observations by existing MF radars. Finally, Section 6 will summarize the achievement and problems encountered in assessing VLF phase perturbations produced by the large mesospheric electric fields.

2.0 TECHNIQUE FOR DETERMINING LARGE MESOSPHERIC ELECTRIC FIELDS

2.1 Instrumentation

The MF radar at the Institute of Space and Atmospheric Studies (ISAS), University of Saskatchewan, Canada provided polarimeter data for the 61 – 67-km altitude range using a 20-μs pulse length at 2.2 MHz during 1979 – 1982. The radar is a single frequency system, but with a large choice of antenna arrays, and is well described in recent papers [e.g., 15]. It is used mainly for wind measurements, but has also provided studies of electron densities using the Differential Absorption Experiment [16].

In Ukraine, the measurements were made with the Kharkiv V. Karazin National University MF radar [17] the specifications for which are as follows: operational frequency band of 1.5–15 MHz, 16-element linearly polarized antenna array of 300 × 300 m^2 physical aperture at f = 1.5–4.5 MHz and of 60 × 60 m^2 at f = 4.5 – 5 MHz, circularly polarized receiving array of two-crossed double rhombus antennas, polarization switch of 22 dB, transmitter peak power of 100 kW, average power of 100 kW, pulse length of 20 μs up to continuous mode, pulse repetition rate of 1 – 100 s^{-1}, receiver dynamic range of 86 dB, IF bandwidth of 60 kHz. The data used in this study were acquired during 1978 through 1997 at frequencies of f = 1.8 – 3.0 MHz using a 25-μs pulse length. The measurements selected for this study were made in the ionospheric D region during conditions disturbed only with respect to large mesospheric electric fields and quiet with respect to all other possible disturbances, when the signals exceeded the noise by a factor of more than five. The observations of the effective electron collision frequency, ν, were made by applying the "Differential Absorption" technique of [18] at the altitudes of 60–66 km.

2.2 Basic Relations

The basic functional relations between the large mesospheric electric field features, ionospheric characteristics, and scattered signal parameters for the quasi-steady case are given by [e.g., 14, 19]

$$R(z)=\frac{\overline{A_-^2}}{\overline{A_+^2}}=\frac{\left[\left(\omega+\omega_L\right)^2+\nu_e^2\right]^2}{\left[\left(\omega-\omega_L\right)^2+\nu_e^2\right]^2}\frac{\left(\omega-\omega_L\right)^2K_\varepsilon^2\left(\frac{\omega-\omega_L}{\nu_e}\right)+\nu_e^2K_\sigma^2\left(\frac{\omega-\omega_L}{\nu_e}\right)}{\left(\omega+\omega_L\right)^2K_\varepsilon^2\left(\frac{\omega+\omega_L}{\nu_e}\right)+\nu_e^2K_\sigma^2\left(\frac{\omega+\omega_L}{\nu_e}\right)}$$
$$\cdot\exp\left\{4K_+(z)-4K_-(z)\right\}, \tag{1}$$

$$K_\pm(z)=\frac{2\pi e^2}{mc}\int_{z_0}^{z}\frac{N(z)\nu_e(z)}{\left(\omega\pm\omega_L\right)^2+\nu_e^2(z)}K_\sigma\left(\frac{\omega\pm\omega_L}{\nu_e(z)}\right)dz=\frac{2\pi}{c}\int_{z_0}^{z}\sigma_{e\pm}(z)dz, \tag{2}$$

$$\sigma_{e\pm}(z)=\frac{e^2N(z)\nu_e(z)}{m\left[\left(\omega\pm\omega_L\right)^2+\nu_e^2(z)\right]}K_\sigma\left(\frac{\omega\pm\omega_L}{\nu_e(z)}\right), \tag{3}$$

$$q_i + \nu_d \lambda N - \nu_a N - \alpha_r (1+\lambda) N^2 = 0, \quad (4)$$

$$q_i - \alpha_r (1+\lambda) N^2 - \alpha_i \lambda (1+\lambda) N^2 = 0, \quad (5)$$

$$\frac{2Q_e}{3kN} - \delta \nu_e (T_e - T_n) = 0, \quad (6)$$

$$j_e = \sigma_e E = const, \quad (7)$$

where

$\overline{A_-^2}$		extraordinary component amplitudes squared and averaged over the sample;
$\overline{A_+^2}$		ordinary component amplitudes squared and averaged over the sample;
$K_{\pm}(z)$		total absorption of the ordinary (+ subscript)and extraordinary (– subscript) scattered signal components, $K_-(z) > K_+(z)$;
$\sigma_{e\pm}$		high frequency electron conductivity for the ordinary and extraordinary components, respectively;
ω	=	$2\pi f$;
f		sounding frequency;
ω_L	=	$2\pi f_L$;
f_L		electron gyrofrequency longitudinal component;
f_L	≈	1.35 MHz for middle latitudes;
$K_\varepsilon^2\left(\frac{\omega \pm \omega_L}{\nu_e}\right)$		coefficient that represents the kinetic effects in the high frequency permittivity [e.g., 20];
$K_\sigma^2\left(\frac{\omega \pm \omega_L}{\nu_e}\right)$		coefficient that represents the kinetic effects in the high frequency conductivity [e.g., 20];
e		electron charge;
m		electron mass;
c		speed of light;
z_0		lower ionospheric boundary altitude that is assumed to be equal to z_0 = 60 km for the daytime and z_0 = 75 – 80 km for the nighttime, in most of the cases;
q_i		ion production rate;
ν_d		effective rate at which negative ions are destroyed by electron detachment;
N		electron number density;
λ	=	N^-/N
N^-		negative ion number density;
ν_a		effective rate at which the negative ions are formed by attachment of electrons to neutral constituents;
α_r		effective rate of electron-ion recombination;
α_I		effective rate of ion-ion recombination;
Q_e/N		mean energy imparted to an electron by an external heating source, e.g., external electric field;
k		Boltzmann's constant;
T_e		electron temperature;
T_n		neutral species temperature;
δ		fractional loss of energy per electron collision with a heavy particle;
ν_e		effective electron-neutral collision frequency;
j_e		density of the current driven by an external atmospheric current source;
σ_e		low-frequency conductivity of the ionospheric *D*-region plasma;
E		quasi-steady vertical mesospheric electric field intensity.

Here, Equation (1) represents the relation between the disturbed *D*-region parameters and the ratio of the squared relative amplitudes of the ordinary and extraordinary components of the scattered signals in the quasi-longitudinal approximation. Equations (4) and (5) are the continuity equations for the electrons and ions, respectively, (6) is the energy equation, and (7) is nonlinear Ohm's law for the quasi-steady large mesospheric electric fields. In writing Equations (4) – (6), it has been assumed that the weakly ionized ionospheric plasma is quasi-neutral, the positive and negative ion temperatures are equal to the neutral constituent temperature, and the effects of transport processes on local disturbances can be neglected [e.g., 14]. In the *D* region

$$Q_e = j_e E = j_e^2 / \sigma_e \,. \tag{8}$$

Also, the following are taken into account [e.g., 20, 21]:

$$\sigma_e = K_\sigma(0)\frac{e^2 N}{m\nu_e}, \tag{9}$$

$$\nu_e = 5.8\times10^{-11} N_n T_e^{5/6}, \tag{10}$$

$$\delta = \delta_0 (T_n / T_e)\ (T_e / T_n < 4),\ \delta = 0.2\ \delta_0\ (4 < T_e / T_n < 15), \tag{11}$$

$$\nu_a = (1.4 \times 10^{-29}\ (300/T_e)\ \exp(100/T_n)\ \exp(-700/T_e)\ N(O_2) + 1.0 \times 10^{-31}\ N(N_2))\ N(O_2), \tag{12}$$

$$\alpha_r \approx 6.0\times10^{-6}\left(\frac{300}{T_n}\right)^{1/2}\left(\frac{T_n}{T_e}\right)^{1/2}, \tag{13}$$

where K_σ = 1.42 [20], N_n is the number density of neutral particles, $N(O_2)$ is the number density of molecular oxygen in cm^{-3}, $N(N_2)$ is the number density of molecular nitrogen in cm^{-3}, T_e and T_n are in K, ν_a in s^{-1}, α_r in $cm^3\ s^{-1}$, the subscript 0 is used to denote the magnitude of the plasma parameters in the absence of large mesospheric electric fields.

When the differential absorption of the two magnetoionic components is neglected in the first, the lowest sample of signals scattered from the layer at the altitude z_1, which is usually true for z_1 < 66 – 69 km for the daytime conditions [e.g., 18], the following relation is derived from (1) for determining the disturbed $\nu_e(z_1)$ value from the measured value $R(z_1)$ [14, 22, 13]:

$$R(z_1) = \frac{\left[(\omega+\omega_L)^2 + \nu_e^2(z_1)\right]^2}{\left[(\omega-\omega_L)^2 + \nu_e^2(z_1)\right]^2} \frac{(\omega-\omega_L)^2 K_\varepsilon^2\left(\frac{\omega-\omega_L}{\nu_e(z_1)}\right) + \nu_e^2(z_1) K_\sigma^2\left(\frac{\omega-\omega_L}{\nu_e(z_1)}\right)}{(\omega+\omega_L)^2 K_\varepsilon^2\left(\frac{\omega+\omega_L}{\nu_e(z_1)}\right) + \nu_e^2(z_1) K_\sigma^2\left(\frac{\omega+\omega_L}{\nu_e(z_1)}\right)} \tag{14}$$

Then, from (6) – (11) it is easy to obtain a relation for the electric field intensity $E(z_1)$ [14, 22]

$$E^2 = \frac{km\delta_0 T_{e0}(z_1)}{0.97e^2}\nu_e^2(z_1)\left\{1-\left(\frac{\nu_{e0}(z_1)}{\nu_e(z_1)}\right)^{6/5}\right\}\ (T_e/T_{e0} \le 4), \tag{15}$$

$$E^2 = \frac{km\delta_0 T_{e0}(z_1)}{4.85e^2}\nu_e^2(z_1)\left\{\left(\frac{\nu_e(z_1)}{\nu_{e0}(z_1)}\right)^{6/5}-1\right\}\ (T_e/T_{e0} > 4), \tag{16}$$

where $T_{e0}(z_1)$ and $\nu_{e0}(z_1)$ are related by (10).

The determination of the current density j = *constant* by using (4) – (16) is a crucial step before the transition to the second layer from which the signals have been scattered. This condition is apparently satisfied in the 60 to 70 – 75-km altitude range (see [12] for a discussion of this subject). The disturbed value of $N(z_1)$ is given by

$$N(z_1) = q_i^{1/2}(z_1)\left\{\left(1+\lambda(\theta_1)\right)\left(\alpha_r(\theta_1)+\lambda(\theta_1)\alpha_i(z_1)\right)\right\}^{-1/2}, \tag{17}$$

which allows the specification of j_e by (7), (9). Here, $\theta_1 = T_e(z_1) / T_{e0}(z_1) = (\nu_e(z_1) / \nu_{e0}(z_1))^{6/5}$. Then, from (6) – (9) the $N(z_2)$ in the second layer is given by

$$N(z_2) = j_e\left\{2.1\times k\frac{e^2}{m}T_{e0}(z_2)\delta(\theta_2)(\theta_2-1)\right\}^{-1/2}. \tag{18}$$

Equating (18) and the expression for $N(z_2)$ derived from (1) gives the following equation for $\nu_e(z_2)$ allowing for the differential absorption of the scattered signals:

$$\begin{aligned} &j_e\left\{2.1\times\frac{e^2}{m}T_{e0}(z_2)\delta(\theta_2)(\theta_2-1)\right\}^{-1/2} \\ &= \ln\left\{R^{-1}(z_2)\frac{\left[(\omega+\omega_L)^2+\nu_e^2(z_2)\right]^2}{\left[(\omega-\omega_L)^2+\nu_e^2(z_2)\right]^2}\frac{(\omega-\omega_L)^2K_\varepsilon^2\left(\frac{\omega-\omega_L}{\nu_e(z_2)}\right)+\nu_e^2(z_2)K_\sigma^2\left(\frac{\omega-\omega_L}{\nu_e(z_2)}\right)}{(\omega+\omega_L)^2K_\varepsilon^2\left(\frac{\omega+\omega_L}{\nu_e(z_2)}\right)+\nu_e^2(z_2)K_\sigma^2\left(\frac{\omega+\omega_L}{\nu_e(z_2)}\right)}\right\} \\ &\cdot\left\{\frac{8\pi e^2}{mc}\nu_e(z_2)\Delta z\left(\frac{K_\sigma\left(\frac{\omega-\omega_L}{\nu_e(z_2)}\right)}{(\omega-\omega_L)^2+\nu_e^2(z_2)}-\frac{K_\sigma\left(\frac{\omega+\omega_L}{\nu_e(z_2)}\right)}{(\omega+\omega_L)^2+\nu_e^2(z_2)}\right)\right\}^{-1} \end{aligned} \tag{19}$$

where Δz is the height increment. Since both the right-hand and left-hand sides of (19) are equal to $N(z_2)$, then the $N(z_2)$ can be easily determined provided the value of $\nu(z_2)$ has been established.

We obtain the following equation for $\nu(z_3)$ in the third layer:

$$\begin{aligned} &j_e\left\{2.1\times\frac{e^2}{m}T_{e0}(z_3)\delta(\theta_3)(\theta_3-1)\right\}^{-1/2} \\ &= \left\{\ln\left\{R^{-1}(z_3)\frac{\left[(\omega+\omega_L)^2+\nu_e^2(z_3)\right]^2}{\left[(\omega-\omega_L)^2+\nu_e^2(z_3)\right]^2}\frac{(\omega-\omega_L)^2K_\varepsilon^2\left(\frac{\omega-\omega_L}{\nu_e(z_3)}\right)+\nu_e^2(z_3)K_\sigma^2\left(\frac{\omega-\omega_L}{\nu_e(z_3)}\right)}{(\omega+\omega_L)^2K_\varepsilon^2\left(\frac{\omega+\omega_L}{\nu_e(z_3)}\right)+\nu_e^2(z_3)K_\sigma^2\left(\frac{\omega+\omega_L}{\nu_e(z_3)}\right)}\right\}-4\left(K_-(z_2)-K_+(z_2)\right)\right\} \\ &\cdot\left\{\frac{8\pi e^2}{mc}\nu_e(z_3)\Delta z\left(\frac{K_\sigma\left(\frac{\omega-\omega_L}{\nu_e(z_3)}\right)}{(\omega-\omega_L)^2+\nu_e^2(z_3)}-\frac{K_\sigma\left(\frac{\omega+\omega_L}{\nu_e(z_3)}\right)}{(\omega+\omega_L)^2+\nu_e^2(z_3)}\right)\right\}^{-1} \end{aligned} \tag{20}$$

where

$$4\left(K_{-}(z_2)-K_{+}(z_2)\right)=\ln\left\{R^{-1}(z_2)\frac{\left[\left(\omega+\omega_L\right)^2+\nu_e^2(z_2)\right]^2}{\left[\left(\omega-\omega_L\right)^2+\nu_e^2(z_2)\right]^2}\frac{\left(\omega-\omega_L\right)^2K_\varepsilon^2\left(\frac{\omega-\omega_L}{\nu_e(z_2)}\right)+\nu_e^2(z_2)K_\sigma^2\left(\frac{\omega-\omega_L}{\nu_e(z_2)}\right)}{\left(\omega+\omega_L\right)^2K_\varepsilon^2\left(\frac{\omega+\omega_L}{\nu_e(z_2)}\right)+\nu_e^2(z_2)K_\sigma^2\left(\frac{\omega+\omega_L}{\nu_e(z_2)}\right)}\right\}$$

is obtained from (1) – (3), (19). The $N(z_3)$ is obtained from (20) as above by using the value of $\nu_e(z_3)$ determined from (20).

Further, the procedure is consecutively repeated until the relative perturbations in the effective electron temperature and collision frequency become much less than unity. Then, the N in the highest layers that are practically undisturbed is determined from (1), (2) by applying the classical differential absorption technique and specifying the value of ν_{e0} [18].

It is important to note that this technique permits not only simultaneous measurements of the height profiles of large mesospheric electric field intensities and the profiles of associated disturbances in the effective collision frequency, the electron temperature and density, but also simultaneous estimates of disturbances in the *D*-region basic parameters ν_a/ν_{a0}, δ/δ_0, α_r/α_{r0}, λ/λ_0, σ/σ_{e0}, and in N^-/N_0^- and N^+/N_0^+. Thus, the developed technique allows remote sensing of a cluster of the D-region parameters disturbed by the large mesospheric electric fields. Unfortunately, an essential deficiency of this technique is the fact that it is applicable only when the strength of the signals scattered from the lower part of the *D* region, 60 – 70 km, is high enough, which does not always occur when the existing MF radars are used.

2.3 Technique

This section illustrates how the technique works in detail. The data selected for this analysis were collected on November 24, 1984 with the MF radar at the Kharkiv V. Karazin National University Radiophysical Observatory (49°38'N, 36°20'E) [e.g., 17]. The radar specifications in this experiment were as follows: 2.3-MHz sounding frequency, 25-μs pulse length, and pulse repetition rate of 1 per second. We have chosen for the analysis the 5-min interval 09:54 – 09:59 LT, which exhibits no time trend in the intensity of the signals scattered from the 66 – 84-km altitude and the signal-to-noise ratio exceeding 8.

After testing the input statistical series of the squared noise amplitudes and of the squared signal plus noise amplitudes for homogeneity and further subtracting the noise from the signal plus noise, the height dependence of $R(z)$ defined in (1) is formed, and the corresponding sample variances $S^2(R)$ are estimated [e.g., 23]:

$$S^2(R)=\frac{\overline{A_-^4}}{\overline{A_+^4}}\left\{\frac{S^2\left(A_-^2\right)}{\overline{A_-^4}}+\frac{S^2\left(A_+^2\right)}{\overline{A_+^4}}-2\rho_{\pm}\frac{S\left(A_-^2\right)}{\overline{A_-^2}}\frac{S\left(A_+^2\right)}{\overline{A_+^2}}\right\} \tag{21}$$

where $S^2\left(A_-^2\right)$, $S^2\left(A_+^2\right)$ represent the sample variance of the extraordinary and ordinary scattered signal components, respectively, $\rho_{\pm}$ is the sample correlation coefficient between the squared extraordinary and ordinary scattered signal components. Equation (21) yields the 99 percent confidence intervals for $R(z)$, which are lying within the range ±2.4% for R(66 km) and ±16% for R(78 km).

Then, the dependence $R(z)$ obtained experimentally is used for simultaneously determining the height dependences of the basic parameters of the disturbed *D* region and the disturbing large mesospheric

electric field characteristics shown in Table 1 where the 0.99 confidence intervals are indicated in parentheses.

First, the ν_e(66 km) is determined by making use of (14) and ν_{e0}(66 km) = 1.68×10^7 s^{-1} that corresponds to an undisturbed electron temperature of T_{e0} = 240 K in the isothermal ionospheric plasma; the model parameter values of the undisturbed medium are borrowed from [20, 21, 24 – 30]. Then, given the ν_e, ν_{e0}, the values of E, T_e/T_{e0}, δ/δ_0, α/α_0, ν/ν_0, λ/λ_0 for z = 66 km are obtained from (10) – (13), (15). Taking into account the high stability of the main ionizing radiations, the cosmic rays, at 66 km under quiet geomagnetic conditions [e.g., 24 – 26, 30, 31]), the electron number density N_0(60 km) can be set equal to 60 cm^{-3} for q_i = 0.05 cm^{-3} s^{-1} (see also [12]). Then, from (4), (5), (12), (13) when $\alpha_{r0} = 6.7 \times 10^{-6}$ cm^{-3} s^{-1}, $\alpha_i = 6.8 \times 10^{-8}$ cm^{-3} s^{-1}, ν_{a0} = 0.7 s^{-1}, ν_d = 0.7 s^{-1}, $\lambda_0 = \nu_{a0}/\nu_d$ = 1.0, we obtain N(66 km), and from (7), (9) we also find the height-independent current density $j_e = 3.58 \times 10^{-8}$ A/m^2 induced by the mesospheric source at $z \geq 66$ km.

The disturbed values of the ionospheric plasma parameters at higher altitudes are determined in the same way as above. The initial values are assumed to be equal to

ν_{e0} (69 km) = 1.1×10^7 s^{-1}, T_{e0} (69 km) = 230 K,

ν_{e0} (72 km) = 6.8×10^6 s^{-1}, T_{e0} (72 km) = 210 K,

ν_{e0} (75 km) = 4.2×10^6 s^{-1}, T_{e0} (75 km) = 200 K.

Table 1 shows that the relative measurement errors in the ionospheric parameters derived from the given experiment data vary within the limits of the order of one percent at z = 66 km to 23% at z = 75 km, as determined for the 99 percent confidence intervals. However, there exist sources of bias errors that require analysis in each specific event, e.g., in this experiment, an additional error of 2% is due to the neglect of the differential absorption at $z \leq 66$ km. In general, the assumed values of ν_{e0} and associated with them T_{e0} (see (10)) also exhibit variations due to seasonal, diurnal, and regional dependences of atmospheric parameters, as well as the atmospheric disturbances from acoustic-gravity waves [e.g., 32]. The errors caused by radar imperfections may not also be excluded altogether in determining ν_e (e.g., inaccuracy in altitude determination). The control and taking account of all possible errors is very difficult. However, Equation (1) shows that each specific sample value of R has an associated interval of ν_{e0} that corresponds to the positive values of N in (1). Therefore, the physical requirement $N \geq 0$ actually imposes a restriction on the maximum possible total bias in determining or assuming the value of ν_{e0}. For example, this kind of error in this experiment is not more than 16%, which corresponds to N = 0 at z = 69 km. The analysis of the Kharkiv MF radar data has revealed that this kind of error attained a maximum value of 38% over the interval 1979 – 1994 only once (probability of 0.005) [13, 22]. The mean was approximately equal to 19%. The inverse proposition is also valid: a limited interval of $R \pm \Delta R$ corresponds to the existing interval of $\nu_{e0} \pm \Delta\nu_{e0}$, which limits the maximum possible bias in determining R; in the given experiment the maximum possible value of $\Delta R / R$ is equal to approximately 16%. Thus, in a specific experiment, there always exist physical constraints for restricting and estimating the maximum possible bias. For example, in this experiment, the bias does not exceed 30% at $z \leq 69$ km and 50% in the interval 69 km < $z \leq$ 75 km, which is in accordance with the results of *Gokov and Martynenko* [22], *Martynenko et al*, [13], and *Martynenko, Rozumenko, and Tyrnov* [12].

As a whole, Table 1 shows that large mesospheric electric fields cause significant, by a factor of up to two times and more, disturbances virtually in all basic parameters of the lower *D*-region plasma, except for the electron number density. The latter is explained by a mutual balance between the processes resulting in a decrease in N due to the attachment of electrons to air molecules and the processes resulting in an increase in N due to a decrease in the effective rate of electron-ion recombination under the influence of large mesospheric electric fields (see (4) – (7), (12), (13)).

Table 1 Parameters of the *D* region disturbed by large mesospheric electric fields.

z (km)	66	69	72	75
ν_e (s^{-1})	$\left[3.15\begin{pmatrix}+0.07\\-0.07\end{pmatrix}\right]\times10^7$	$\left[2.51\begin{pmatrix}+0.22\\-0.29\end{pmatrix}\right]\times10^7$	$\left[6.90\begin{pmatrix}+0.10\\-0.10\end{pmatrix}\right]\times10^6$	4.2×10^6
E (V/m)	$0.46\begin{pmatrix}+0.02\\-0.02\end{pmatrix}$	$0.40\begin{pmatrix}+0.04\\-0.07\end{pmatrix}$	$0.02\begin{pmatrix}+0.01\\-0.01\end{pmatrix}$	0
ν_e / ν_{e0}	$1.88\begin{pmatrix}+0.05\\-0.05\end{pmatrix}$	$2.29\begin{pmatrix}+0.19\\-0.27\end{pmatrix}$	$1.01\begin{pmatrix}+0.01\\-0.01\end{pmatrix}$	1.0
T_e/T_{e0}	$2.13\begin{pmatrix}+0.06\\-0.06\end{pmatrix}$	$2.70\begin{pmatrix}+0.28\\-0.38\end{pmatrix}$	$1.01\begin{pmatrix}+0.01\\-0.01\end{pmatrix}$	1.0
δ/δ_0	$0.47\begin{pmatrix}+0.01\\-0.01\end{pmatrix}$	$0.37\begin{pmatrix}+0.06\\-0.03\end{pmatrix}$	$0.99\begin{pmatrix}+0.01\\-0.01\end{pmatrix}$	1.0
N (cm^{-3})	$60\begin{pmatrix}+1\\-2\end{pmatrix}$	$60\begin{pmatrix}+5\\-12\end{pmatrix}$	$350\begin{pmatrix}+50\\-60\end{pmatrix}$	$400\begin{pmatrix}+90\\-80\end{pmatrix}$
ν_a / ν_{a0}	$1.95\begin{pmatrix}+0.06\\-0.06\end{pmatrix}$	$2.15\begin{pmatrix}+0.03\\-0.05\end{pmatrix}$	1.0	1.0
α_r/α_{r0}	$0.69\begin{pmatrix}+0.01\\-0.01\end{pmatrix}$	$0.61\begin{pmatrix}+0.05\\-0.03\end{pmatrix}$	1.0	1.0
λ/λ_0	$1.95\begin{pmatrix}+0.06\\-0.06\end{pmatrix}$	$2.15\begin{pmatrix}+0.03\\-0.05\end{pmatrix}$	1.0	1.0
N/N_0	$1.00\begin{pmatrix}+0.01\\-0.03\end{pmatrix}$	$1.11\begin{pmatrix}+0.09\\-0.22\end{pmatrix}$	1.0	1.0
N^- / N_0^-	$1.95\begin{pmatrix}+0.01\\-0.04\end{pmatrix}$	$2.39\begin{pmatrix}+0.13\\-0.45\end{pmatrix}$	1.0	1.0
N^+ / N_0^+	$1.50\begin{pmatrix}+0.01\\-0.04\end{pmatrix}$	$1.47\begin{pmatrix}+0.11\\-0.28\end{pmatrix}$	1.0	1.0
σ_e/σ_{e0}	$0.53\begin{pmatrix}+0.02\\-0.03\end{pmatrix}$	$0.48\begin{pmatrix}+0.01\\-0.04\end{pmatrix}$	$0.99\begin{pmatrix}+0.01\\-0.01\end{pmatrix}$	1.0

The technique developed for remotely sensing large mesospheric electric fields can briefly be summarized as follows:

(i) The $\nu_e(z_1)$ is determined by using (14) in the first lowest layer at z_1 < 66 – 69 km from which the signals have been received,

(ii) The $T_e(z_1)/T_{e0}(z_1)$ is specified by using the $\nu_e(z_1)$ and (10),

(iii) The $E(z_1)$ is determined by using (15) or (16) depending on the value of $T_e(z_1) / T_{e0}(z_1)$,

(iv) The $N(z_1)$ is calculated by using (17),

(v) The current density j_e = constant for the source of large mesospheric electric fields is determined from (7) and (9),

(vi) The $\nu_e(z_2)$ is determined for the second layer of the scattered signals from (19) and then the $N(z_2)$ is determined,

(vii) The $E(z_2)$ is determined from (7) and (9),

(viii) The $\nu_e(z_3)$ is determined in the third layer of the scattered signals from (20) and then the $N(z_3)$ is determined,

(ix) The $E(z_3)$ is determined from (7) and (9),

(x) Further, the procedure is consecutively repeated by using equation (20) and relations (7), (9) until the relative disturbances in the electron temperature and effective collision frequency become much less than unity; at higher altitudes the medium can be considered undisturbed and the values of E small, i.e., close to zero.

Hence, the set of theoretical relations (1) – (17) provides the framework for modeling studies of how large mesospheric electric fields affect the ionospheric *D*-region parameters. The disturbances in the electron temperature and effective collision frequency (see Equations (10), (15), (16)) are the primary cause of disturbances in other parameters. In particular, Equations (1), (14) describe disturbances in the ratio of the squared amplitudes of the ordinary and extraordinary components of the scattered signals. Equation (2) governs variations in the total absorption of MF radio signals. Equation (3) permits the determination of disturbances in the HF conductivity of the ionospheric plasma. Equation (7) relates the large mesospheric electric fields and the low-frequency electron conductivity of the plasma. Equation (8) takes account of the large mesospheric electric field energy losses via Joule heating. Equation (10) provides the relationship between disturbances in the electron temperature and the effective collision frequency. Equation (11) establishes disturbances in the fractional loss of energy per electron collision with a heavy particle. Equation (12) is used to calculate the effective rate at which the negative ions are formed by the attachment of electrons to neutral constituents. Equation (13) shows disturbances in the effective rate of electron-ion recombination. Equation (17) defines explicitly disturbances in the electron number density.

Generally, the theoretical model outlined above forms the basis for the technique of *Martynenko* [19] for clustered-technique remote sensing of processes coupling the electrically active mesosphere with the ionospheric *D*-region plasma, the accuracy of which is not inferior to the corresponding in situ rocket techniques [e.g., 33] but offers considerable cost benefits. A significant extension to the earlier technique of *Gokov and Martynenko* [22] and *Martynenko et al*. [13] has been achieved by using the model representation of the source of large mesospheric electric fields as the current source [12]. It includes the extension of the altitude range and permits the simultaneous measurements of large mesospheric electric fields and charged particle number densities. The minimum total error of the suggested method is approximately 20% and the maximum total error can attain a value of 40 – 50%, while the particular error magnitudes need to be specified in each particular experiment. The above-mentioned errors can be reduced by roughly 2 times if independent measurements of the neutral temperatures in the mesosphere were provided, e.g., by the lidar techniques [34].

Thus, there are good grounds for the conclusion that further development and implementation of the remote sensing techniques will reduce an acute shortage of data on the electrodynamic processes acting in the electrically active mesosphere and on the mesosphere's coupling to other atmospheric and ionospheric regions. These techniques will permit simultaneous measurements of large mesospheric electric fields and disturbed lower ionospheric parameters.

2.4 Large Mesospheric Electric Field Measurements

This section briefly summarizes the main results inferred thus far from MF radar electric field measurements taken in Canada and Ukraine [9, 10, 11]. Below, we characterize the database, illustrate

temporal variability, and present the statistical analysis of the large mesospheric electric fields, electron temperatures, and the effective collision frequencies.

2.4.1 Database

The estimates of VLF phase variations require the characterization of the temporal and 3-dimensional variability of the ionospheric conduction contours. However, the ionospheric observations have so far been made with monostatic MF radars with antennas forming wide fixed vertical beams and thus capable of measuring only a one-dimensional distribution of ionospheric parameters. The horizontal variability remains generally unknown. Consequently, the available MF radar database is insufficient to characterize the lower ionospheric boundary in detail in order to compute VLF phase variations.

The database of MF radar measurements is developed in a series of campaigns carried out in Ukraine between 1978 – 1994 and in Canada between 1979 – 1982. The large mesospheric electric field and the effective electron collision frequency, ν, data were taken from the 60 – 66 km altitude range at Kharkiv V. Karazin National University and from the 61 – 67 km range at the Institute of Space and Atmospheric Studies (ISAS), University of Saskatchewan, Canada. The Ukrainian MF radar operated at 1.8 – 3.0-MHz, and acquired n = 185 measurements of 5 – 10 min in duration each [13, 22]. The Canadian MF radar operated at 2.2 MHz, and collected n = 170 measurements of 10 min in duration each. Thus, the total MF radar database contains 385 MF radar measurements, which exceeds by a factor of a few times the total rocket database.

2.4.2 Temporal Variability

The variability of large mesospheric electric fields displays a wide range of time scales, from an order of one minute (as shown in Figure 1 in [10]) to an order of an hour, as shown in Figure 2 for Ukraine (probing frequency of f = 2.3 MHz) and in Figure 3 for Canada (f = 2.2 MHz).

However, the database consists of separate 5 – 10 min intervals of measurements collected over the years and the temporal variability they provide is not continuous. The continuity of measurements may be improved by either upgrading the existing MF radars or constructing new radars in order to increase the signal-to-noise ratio.

2.4.3 The Distribution of the Effective Electron Collision Frequencies

The effective electron collision frequency, ν, is the primary plasma parameter that is used for deriving both the electric fields and the low-frequency conductivities. Preliminary data analysis includes the estimate of the histogram showing the distribution of ν / ν_m where ν_m is a model value of ν in the absence of large mesospheric electric fields at heights from which the scattered signals were received. Allowing for the kinetic effects, as *Gokov and Martynenko* [22] and *Martynenko et al.* [14] assumed, $\nu_m = 3.75 \times 10^7$ s^{-1} at z = 60 km, $\nu_m = 3.32 \times 10^7$ s^{-1} at z = 61 km, $\nu_m = 2.55 \times 10^7$ s^{-1} at z = 63 km, $\nu_m = 2.21 \times 10^7$ s^{-1} at z = 64 km, $\nu_m = 1.68 \times 10^7$ s^{-1} at z = 66 km, and $\nu_m = 1.47 \times 10^7$ s^{-1} at z = 67 km. The histograms showing the distribution of ν / ν_m values are presented in [10] (Figure 3 from the Ukrainian data and Figure 4 from

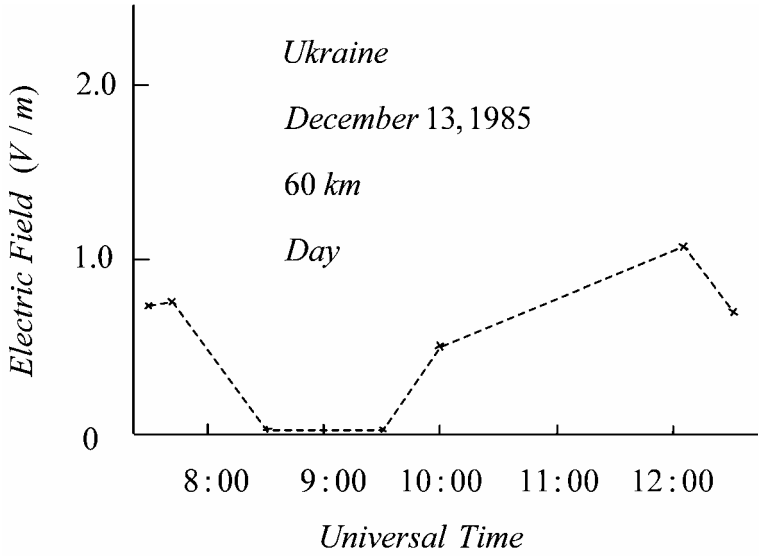

Figure 2. A representative time dependence of large mesospheric electric fields obtained in Ukraine.

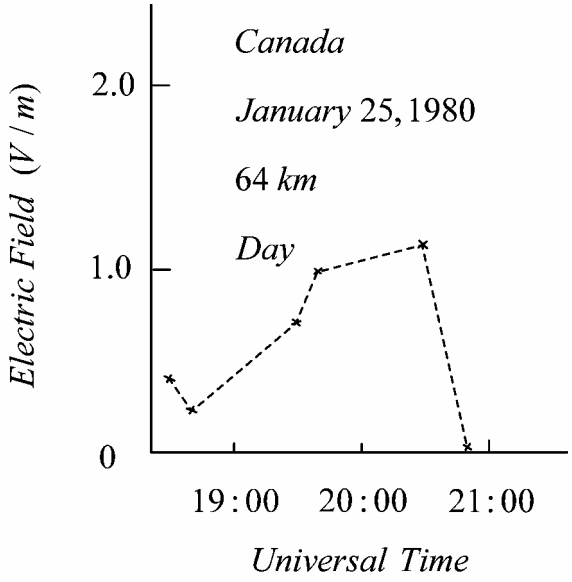

Figure 3. A representative time dependence of large mesospheric electric fields obtained in Canada.

the Canadian data). It is obvious that the ν / ν_m sample in the absence of large mesospheric electric fields should have a Gaussian distribution with a mean of $M[\nu / \nu_m] = 1$. This provides the reason for suggesting that the values $\nu / \nu_m < 1$ are associated with cases when large mesospheric electric fields are absent, and these data are excluded from the database of the ν / ν_m measurements that are used for determining large mesospheric electric field effects. Furthermore, the symmetry of the Gaussian distribution of ν / ν_m about $\nu / \nu_m = 1$ in the absence of large mesospheric electric fields provides another criterion for excluding the undisturbed component with $\nu / \nu_m > 1$ from the analysis.

2.4.4 The Distribution, w_E, of the Large Mesospheric Electric Fields

The histograms for the distribution, w_E, of the large mesospheric electric fields, E are shown in [10] (Figure 5 for the Ukrainian and Figure 6 for Canada). There, $w_E = n_i /(n\ \Delta E)$, i is a cell number, i = 1,…,13, n_i is the number of samples of E that lie within the $(i-1)\ \Delta E < E \leq (i\ \Delta E)$ cell, ΔE = 0.5 V/m is the width of each cell, n = 139 (Ukraine) and n = 120 (Canada) are the sample sizes. Within the 0.99 confidence interval, the histograms exhibit the possibility of dividing them into two parts: that constituting the main body of $0 < E \leq 2.5$ V/m, n = 129 for the Ukrainian data and n = 99 for the Canadian data, and that constituting the tail $E > 2.5$ V/m, n = 10 for the Ukrainian data and n = 21 for the Canadian data. Also, within the 0.99 confidence interval estimated by making use of Pearson's test, the main body corresponds to a one-parameter Rayleigh probability density functions as given by

$$f(E) = \frac{E}{\sigma^2} e^{-\frac{E^2}{2\sigma^2}} \tag{22}$$

where $\sigma = E_m$ is the most probable value of E, $M_1[E] = (\pi / 2)^{1/2}\ \sigma$ is the mean, $M_2[E] = 2\ \sigma^2$ is the second ordinary moment for a Rayleigh set, and $D\ [E] = (2 - \pi / 2)\ \sigma^2$ is the variance. Within the same 0.99 confidence interval, the Rayleigh part of the histogram in [10] (Figure 5) provides an estimate of $M_1[E]$ = 0.72 ± 0.11 V/m where the sample mean $< E_R > = 0.72$ V/m, which corresponds to $\sigma = 0.57$ V/m. The corresponding histogram w_E for large mesospheric electric field intensities constructed by using n = 129 samples and the theoretical Rayleigh probability density function are presented for Ukraine in [10] (Figure 7). The similar histogram for Canada is presented in [10] (Figure 8) where, $M_1[E]$ = 0.89 ± 0.12 V/m, $< E_R >$ = 0.89 V/m, and σ = 0.71 V/m.

Hence, at least two mechanisms for generating large mesospheric electric fields should exist. The Rayleigh distribution of E can be formed as a result of the summation of the random fields from a large number of primary small-scale mesospheric generators. The possible mesospheric processes resulting in such small-scale active elements have been discussed, e.g., by *Goldberg* [3] and *Polyakov et al.* [6]. The processed data have shown that the probability of occurrence of such an integral Rayleigh mesospheric generator is equal to approximately 70% for Ukraine and approximately 58% for Canada, and the probability of the lack of large mesospheric electric fields is about 25% for Ukraine and approximately 30% for Canada.

Unfortunately, the number of observations occurring in the sample interval $E > 2.5$ V/m is equal to n = 10 with the probability of occurrence of approximately 5% for Ukraine (see Figure 5 in [10]) and n = 21 with the probability of occurrence of approximately 12% for Canada (see Figure 6 in [10]). This dataset is too small to draw statistical inferences from, and these data are barely adequate for characterizing a mean of $< E >$ = (4.3 ± 1.3) for Ukraine and $< E >$ = (4.4 ± 0.4) for Canada within the 0.90 confidence interval.

Generally, the upper limit for E is determined by an atmospheric breakdown threshold of $E_t = 218 \times (p / p_0)$ kV/m (here p is the atmospheric pressure at the altitude z, p_0 is the atmospheric pressure at sea level [e.g., 35]). For example, E_t = 50 – 10 V/m within the altitude range of z = 60 – 70 km, respectively. The fields exceeding this threshold are associated with red sprite, blue jet, and elf phenomena in the middle atmosphere.

2.4.5 Seasonal Dependencies in the Statistical Parameters of Large Mesospheric Electric Fields

To detect a possible seasonal dependencies in the statistical parameters of large mesospheric electric fields, all the data in the database were arbitrary divided into two subsets: "winter" (September 24 – March 23) and "summer" (March 24 – September 23). Then the Rayleigh components in the E distribution were constructed, with n = 69 for the winter and n = 60 for the summer for Ukraine and n = 49 for the winter

and n = 50 for the summer for Canada. The corresponding histograms showing the distributions of w_E and the theoretical Rayleigh distributions are presented in [10] (Figure 11 and Figure 12 for Ukraine and Figure 13 and Figure 14 for Canada). Within the 0.99 confidence interval, in accordance with the Pearson's test, the histograms of w_E correspond to Rayleigh probability density functions with $< E_R >$ = 0.70 V/m and σ = 0.56 V/m for the winter, and $< E_R >$ = 0.75 V/m and σ = 0.60 V/m for the summer for Ukraine. For Canada, $< E_R >$ = 0.91 V/m and σ = 0.73 V/m for the winter, and $< E_R >$ = 0.86 V/m and σ = 0.69 V/m for the summer. It can be seen that that the seasonal differences have turned out to be statistically insignificant. The E > 2.5 V/m values were also occasionally observed during both the winter (n = 6 for Ukraine and n = 11 for Canada) and the summer (n = 4 for Ukraine and n = 10 for Canada).

Generally, this may indicate that the mean local seasonal variations in mesospheric parameters, for example, due to the mean local thunderstorm activity do not exert a noticeable effect at least on the mean performance of the Rayleigh generator of large mesospheric electric fields.

2.4.6 Diurnal Dependence in the Large Mesospheric Electric Field Statistics

An attempt has been made to reveal a diurnal dependence in the large mesospheric electric field statistics in [10]. The histograms for the Canadian data (Figures 15 and 16 in [10]) that show the distribution of w_E are fitted with theoretical Rayleigh distributions for the day (n = 72, $< E_R >$ = 0.91 V/m, σ = 0.73 V/m) and for the night (n = 27, $< E_R >$ = 0.86 V/m, σ = 0.69 V/m), respectively. A comparison of these results indicates the absence of a noticeable diurnal dependence of the distribution function of large mesospheric electric field values.

2.4.7 Distribution Functions for the Relative Disturbances in the Effective Electron Collision Frequencies and in the Electron Temperatures

The distributions of the effective electron collision frequencies and the electron temperatures are reflected in the distributions of disturbances in the low-frequency electron conductivity of the plasma.

For the Rayleigh distribution of large mesospheric electric fields, Equation (22), we have derived the theoretical distribution functions $f(\eta)$ and $f(\theta)$ for the relative disturbances in the effective electron collision frequency $\eta = \nu_e / \nu_{e0}$ and in the electron temperature $\theta = T_e / T_{e0}$ by making use of the deterministic functional dependences in Equations (10), (16), as given by

$$f(\eta) = \frac{S_1}{\sigma^2}\left(\eta - \frac{2}{5}\eta^{-1/5}\right)\exp\left\{-\frac{S_1}{2\sigma^2}\left(\eta^2 - \eta^{4/5}\right)\right\}, \tag{23}$$

$$f(\theta) = \frac{S_1}{6\sigma^2}\left(5\theta^{2/3} - 2\theta^{-1/3}\right)\exp\left\{-\frac{S_1}{2\sigma^2}\theta^{2/3}(\theta - 1)\right\}, \tag{24}$$

where $S_1(z) = \left(km\delta_0 T_{e0}\nu_{e0}^2\right)/\left(0.97e^2\right)$, $f(\eta)$ = 0 for η = 1, $f(\theta)$ = 0 for θ =1, and σ is the standard parameter of the primary Rayleigh distribution of large mesospheric electric fields.

Using n = 99 samples of the effective electron collision frequency collected in the height range 61 – 67 km in Canada, the histogram showing the w_η distribution of the disturbances in the effective electron collision frequency is constructed (Figure 3 in [9]). This histogram gives an estimate of the η-distribution first ordinary moment $M_1[\eta]$ = 2.42 ± 0.23 within the 0.98 confidence interval for the 60 – 67-km altitude range. These data have been used for inferring the electric fields whose distribution is presented in [9] (Figure 6). The fitted theoretical distributions $f(\eta)$, Equation (23), have the following parameters: S_1 / σ^2 =

0.54 and $\nu_{e0} = 3.32 \times 10^7$ s^{-1} for 61 km, $S_1 / \sigma^2 = 0.54$ and $\nu_{e0} = 2.21 \times 10^7$ s^{-1} for 64 km, $S_1 / \sigma^2 = 0.18$ and $\nu_{e0} = 1.47 \times 10^7$ s^{-1} for 67 km.

Using $n = 129$ samples of the effective electron collision frequency collected at the altitudes of 60-km, 63-km, and 66-km altitude over Kharkiv (Ukraine), the histogram showing the w_η distribution of the disturbances in the effective electron collision frequency is constructed in a similar fashion (Figure 4 in [9]). This histogram gives an estimate of the η-distribution first ordinary moment $M_1[\eta] = 2.02 \pm 0.14$ within the 0.98 confidence interval for the 60 – 66-km altitude range. The fitted theoretical distributions $f(\eta)$, Equation (23), have the following parameters: $S_1 / \sigma^2 = 0.94$ and $\nu_{e0} = 3.75 \times 10^7$ s^{-1} for 60 km, $S_1 / \sigma^2 = 0.84$ and $\nu_{e0} = 2.55 \times 10^7$ s^{-1} for 63 km, $S_1 / \sigma^2 = 0.45$ and $\nu_{e0} = 1.68 \times 10^7$ s^{-1} for 66 km. These data have been used for inferring the electric fields whose distribution is presented in [9] (Figure 5).

The same datasets are used to construct histogram showing the distribution of the disturbances in the electron temperature, w_θ. The θ-distribution first ordinary moment $M_1[\theta]$ for Canada is equal to 2.91 ± 0.33, and 2.35 ± 0.19 for Ukraine [9].

The analysis of the data on the relative disturbances in the effective electron collision frequencies and in the electron temperatures shows that the large mesospheric electric fields from the Rayleigh generator maintain the electrons in the lower part of the ionospheric D region at elevated temperatures, a factor of 2 higher than T_{e0} and the neutral temperatures T_n. Within the 0.98 confidence interval, the disturbed T_e and ν_e values at higher geomagnetic latitudes are, on average, higher than at mid geomagnetic latitudes. The information on temperatures is of major importance in determining chemical reactions rates.

3.0 MODELING DISTURBANCES IN CONDUCTIVITY PROFILES

The accuracy of maritime navigation systems using very low frequency signals, such as Omega, depends on knowing accurately the altitude of the bottom of the ionosphere. It is well known that rapid vertical changes in this boundary during solar flares and geomagnetic storms can introduce errors of several kilometers in location determinations.

Since the phenomenon of large mesospheric electric fields is supposed to be local and random, this leads us to expect that the surface of reflection is a rough statistical surface.

The large mesospheric electric fields create disturbances in the mesospheric conductivity that is governed by equations (4) – (13). This section briefly summarizes numerical simulations of the conductivity disturbances. The starting point for modeling is the profile of an electric field. The distribution of the large mesospheric electric fields, presented in Section 2.4.4, shows two parts, the main body of $0 < E \leq 2.5$ V/m, and the tail of $E > 2.5$ V/m. The main body corresponds to a one-parameter Rayleigh probability density function. The dataset for the tail is too small to draw statistical inferences, and therefore, these electric fields have to be modeled by rocket measurements presented in Figure 1. Since the statistical analysis presented in Section 2.4.6 shows that the distribution function of large mesospheric electric field values does not exhibit a noticeable diurnal dependence, the same electric field profile may be used to model daytime and nighttime conditions. Accordingly, the mesospheric electric fields have been modeled by two profiles, along with the corresponding electron density profiles.

3.1 Electric Fields in the $0 < E \leq 2.5$ V/m Range

The electric field profile representing the main body of the electric field distribution $0 < E \leq 2.5$ V/m at the lower ionospheric boundary at midlatitudes [10] is shown in Figure 4. Here, the electric field intensities do not exceed 1 V/m.

Figure 5 depicts the profile of the low-frequency conductivity, $\sigma_e(z)$, disturbed by large mesospheric electric fields presented in Figure 4 under daytime conditions as compared to the undisturbed profile, $\sigma_{e0}(z)$, shown as dashed line.

Under nighttime conditions, the same electric field profile in Figure 4 would produce the disturbances in the low-frequency conductivity profile, $\sigma_e(z)$, shown in Figure 6.

The important feature to note is that although the electric field of magnitude below 1 V/m may reduce the low-frequency conductivity at the lower ionospheric boundary by 50% under both daytime and nighttime conditions, it is unable to produce a local minimum in the conductivity profile $\sigma_e(z)$.

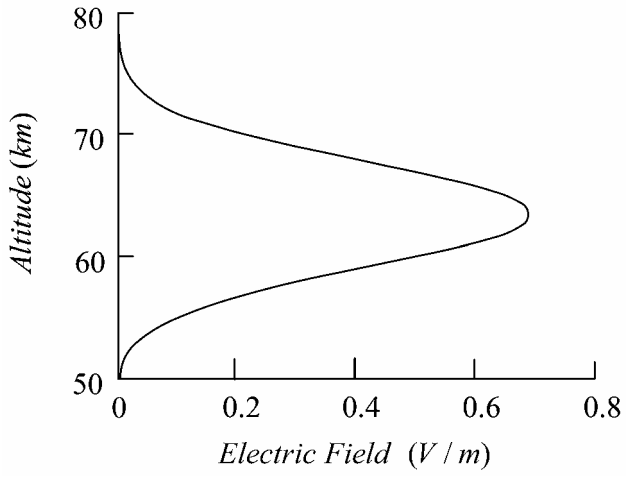

Figure 4. The electric field profile representing the main body of the electric field distribution $0 < E \leq 2.5$ V/m at the lower ionospheric boundary at midlatitudes, as inferred from the Ukrainian MF radar data.

3.2 Electric Fields in the $E > 2.5$ V/m Tail

Figure 7 shows the profile of the low-frequency conductivity, $\sigma_e(z)$, disturbed by the large mesospheric electric fields presented in Figure 1 under daytime conditions as compared to the undisturbed profile $\sigma_{e0}(z)$.

The same electric field profile under nighttime conditions would produce the disturbances in the low-frequency conductivity shown in Figure 8.

The low-frequency conductivities and their disturbances by the electric fields of several volts/meter magnitude for daytime and nighttime conditions differ by orders of magnitude; however, their respective magnitudes not only reduce by a factor of a few times, but also exhibit a local height minimum.

3.3 Conclusions

The simulations illustrated above demonstrate that temporal variability in the large mesospheric electric fields may produce spatial variability in the conductivity contours. If the large mesospheric electric fields exhibit peak intensity above 60 km, then a peak of 1 V/m gives a local rise in the conductivity contour heights by nearly 6 km, while a 4 V/m peak intensity results in a local 10-km upward shift. It is important to notice that the disappearance of the large mesospheric electric fields causes the lowering of the ionospheric conduction contours by the same amount.

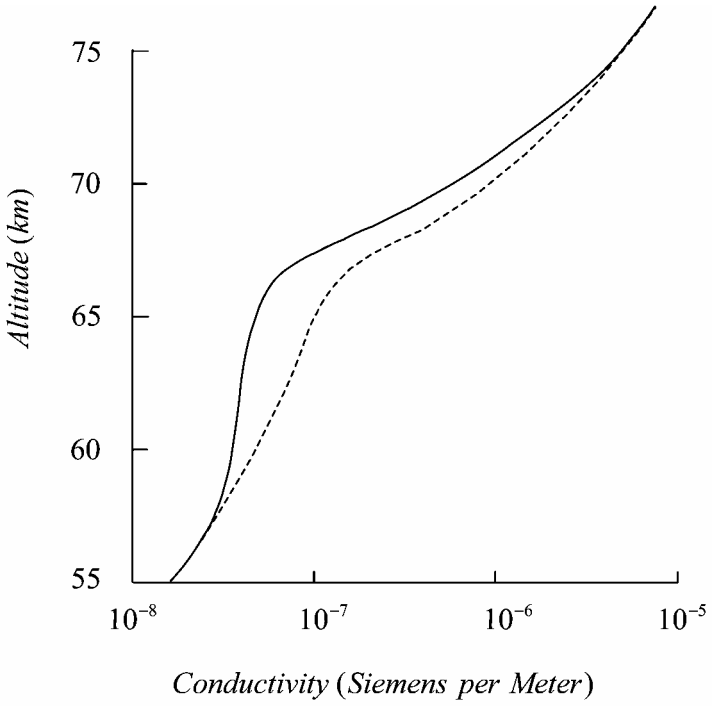

Figure 5. The profile of the low-frequency conductivity disturbed (solid line) by the large mesospheric electric fields with the 1 V/m peak shown in Figure 4 under daytime conditions and the undisturbed (dashed line) conductivity profile.

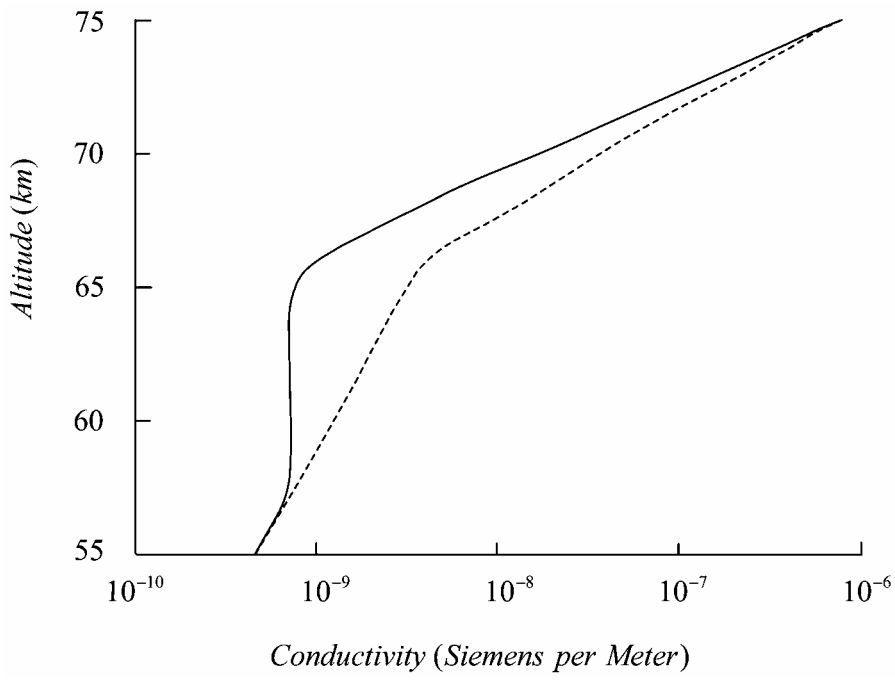

Figure 6. The profile of the low-frequency conductivity disturbed (solid line) by the large mesospheric electric fields with the 1 V/m peak shown in Figure 4 under nighttime conditions and the undisturbed (dashed line) conductivity profile.

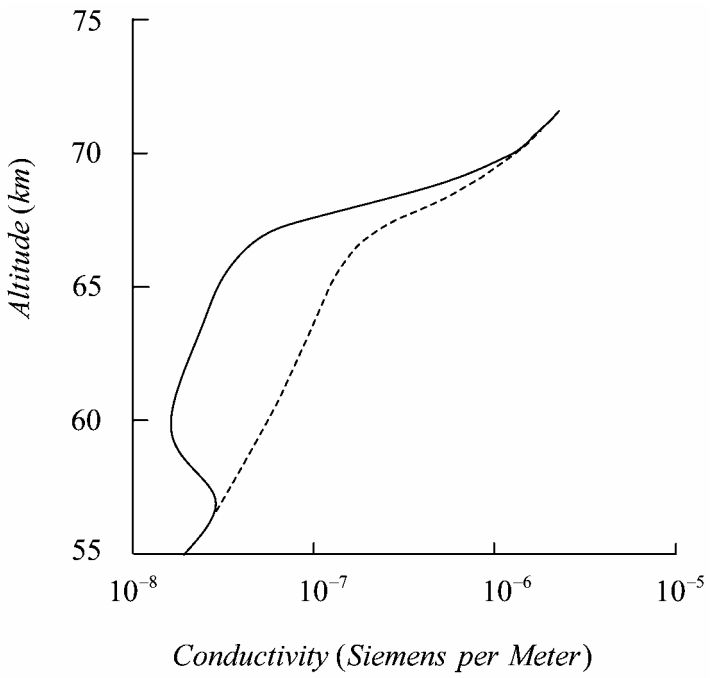

Figure 7. The profile of the low-frequency conductivity disturbed (solid line) by the large mesospheric electric fields with the 4 V/m peak shown in Figure 1 and the undisturbed (dashed line) conductivity profile under daytime conditions.

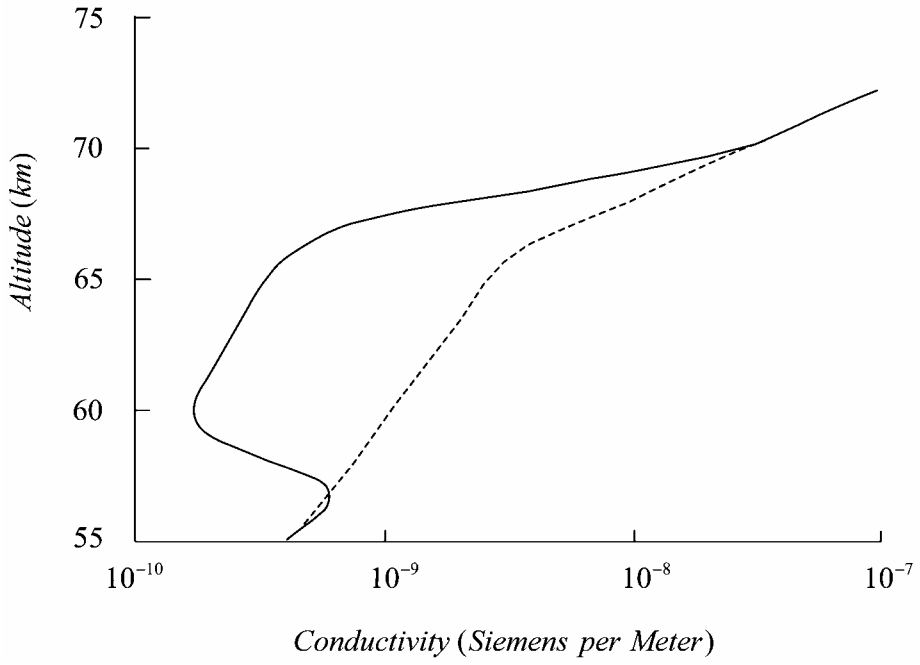

Figure 8. The profile of the low-frequency conductivity disturbed (solid line) by the large mesospheric electric fields with the 4 V/m peak shown in Figure 1 and the undisturbed (dashed line) conductivity profile under nighttime conditions.

4.0 VLF PHASE PERTURBATIONS PRODUCED BY LARGE MESOSPHERIC ELECTRIC FIELDS

The calculations of VLF phase variations require 3D models of the ionospheric conduction contours, which remain unknown. Therefore, this section is concerned with the most logical ways to proceed.

4.1 Smooth Reflective Surface

Since the data collected thus far provide only a one-dimensional view of the vertical variability in the level of reflection, the VLF phase perturbations could be assessed correctly only if the reflective surface is smooth. If the mean height of reflection h changes by an amount Δh, the corresponding phase change $\Delta\phi$ over long distances can be given (in radians) by [36]

$$\Delta\phi = -\frac{2\pi d}{\lambda}\left(\frac{h}{2a}+\frac{\lambda^2}{16h^2}\right)\frac{\Delta h}{h} \tag{25}$$

where d is the great circle distance of the receiver from the transmitter, and a is the radius of the Earth. The wavelength, λ, of special interest is approximately equal to 30 km, while vertical excursions in the contours of constant conductivity due to the large mesospheric electric fields are estimated to be less than 10 km. This way of thinking was employed in interpreting the VLF phase variations (at 16 kHz) attributed to variations in the large mesospheric electric fields during the escape of radioactive materials [37].

4.2 Statistically Rough Reflective Surface

If the contours of constant conductivity that determine the phase fluctuations of the reflected VLF signals are statistically rough surfaces, then the determination of the fluctuations of the signal parameters require numerical information on the character of surface irregularity. The theory of wave scattering from statistically rough surfaces requires information at least about the correlation functions of the deviations of reflective surface from the smooth surface [38]. It is therefore evident that in order to adequately determine the effects of large mesospheric electric fields on radiowave propagation, the variations in the surfaces of constant VLF reflectivity must be studied and specified much more accurately.

However, the MF radars used so far do not permit the determination of the three-dimensional distribution of electric fields and do not provide continuous real-time observations of large mesospheric electric fields. The first restriction is due to the MF radar antennas forming wide fixed vertical beams and thus capable of measuring only a one-dimensional distribution of ionospheric parameters. The second restriction is due to the low signal-to-noise ratios, and consequently, a new MF radar facility should provide higher signal-to-noise ratios.

Thus, a challenge for VLF phase calculations will be to characterize three-dimensional variations in the electric fields intrinsic to the mesosphere. Consequently, this task presents a challenge for the construction of an MF radar facility capable of studying the three-dimensional nature of large mesospheric electric fields.

The engineering solution to the problem of determining a 3-dimentianal distribution of scattered signals in the MF frequency band has yet to be found. At least two ways of obtaining this solution may be indicated. First, a 3-dimentianal distribution could be provided by a new radar capable of performing elevation and azimuth scans. A simpler, but not a necessarily better, solution may be a few relocatable MF radars that may be relocated in response to new knowledge and understanding of the determining factors underlying mesospheric electrodynamics.

5.0 CLUSTERED INSTRUMENT STUDIES

Since the construction of the new MF radar facility requires funds, which are not available at present, joint co-located MF radar and VLF propagation measurement campaigns may provide some information useful for practical applications. It is evident that one-hop VLF circuits with an MF radar below the region where the ray is reflected may yield new advances in VLF phase perturbation research. The Kharkiv V. N. Karazin National University developed, produced, and used relocatable MF radars in numerous clustered instrument measurement campaigns at high and middle latitudes in the U.S.S.R. [17].

However, the electrodynamics of the mesosphere is one of the most poorly understood topics, and its studies involve mesospheric winds and complicated chemistry of the mesosphere and of the ionospheric D region. These studies require coordinated efforts of the entire scientific community who could utilize all radio and optical techniques and computer simulations to cover a wide variety of ionospheric conditions.

6.0 CONCLUSION

The analysis of the complex nature of the problems encountered in assessing VLF phase perturbations produced by the large mesospheric electric fields has provided the following inferences.

The large mesospheric electric fields act to produce local height variations in the ionospheric conduction contours of the order of a few kilometers.

A major achievement in this area has been the development of the MF radar technique for sensing the large mesospheric electric fields remotely.

The MF radars used so far have two restrictions. The minor restriction is low levels of the signal-to-noise ratio in the 60–70 km altitude range, particularly under nighttime conditions, whereas the technique requires the signal-to-noise ratio to be equal or greater than about five. An increase in the signal-to-noise ratio is the way to continuously monitor large mesospheric electric fields.

The fundamental restriction is the fact that the existing MF radars provide only one-dimensional distribution of the electric fields, while the modeling of VLF phase perturbations requires information on the 3-dimensional variability of the ionospheric conduction contours. The absence of the 3-dimensional distribution of the large mesospheric electric fields is the major obstacle to progress in studying VLF phase perturbations. Therefore, the most important challenge for the future will be to develop an MF radar facility capable of determining a 3-dimentianal distribution of scattered signals in the MF frequency band. The data this facility will acquire in some area of the Earth would be sufficient to model VLF phase perturbations produced by the large mesospheric electric fields in that area.

Eventually, an overall understanding of the dynamics and mesospheric and ionospheric D-region chemistry, which establish conductivity patterns, can be achieved by the combined efforts of the entire scientific community.

Meanwhile, one-hop VLF circuits with an MF radar below the region where the ray is reflected may yield new advances in VLF phase perturbation research and provide some information useful for practical applications.

7.0 REFERENCES

[1] Goldberg, R. A., Middle atmospheric electrodynamics: status and future, *J. Atm. Terr. Phys.*, Vol. 46 No. 11, pp. 1083 – 1101, 1984.

[2] Goldberg, R. A., Electrodynamics of the high latitude mesosphere, *J. Geophys. Res.*, Vol. 94, No. D12, pp. 14661 – 14672, 1989.

[3] Goldberg, R. A., Middle atmospheric electrodynamics during MAP, *Adv. Space Res.*, Vol. 10, No. 10, pp. 209 – 217, 1990.

[4] Maynard, N. C., C. L. Croskey, J. D. Mitchell, and L. C. Hale, Measurement of volt/meter electrical fields in the middle atmosphere, *Geophys. Res. Lett.*, Vol. 8, 923, 1981.

[5] Curtis, S. A., Current-driven large horizontal electric fields in the middle atmosphere, in: *IAGA Abstracts, IUGG 19th General Assembly*, Vancouver, B. C., Canada (1987), p. 511.

[6] Polyakov, S. V., V. O. Rapoport, and V. Yu. Trakhtengerts, On the generation of electric fields in the upper atmosphere (in Russian), *Geomagnetism and Aeronomy*, Vol. 30, No. 5, pp. 869 – 871, 1990.

[7] Aikin, A. C., and N. C. Maynard, A Van de Graaf source mechanism for middle atmospheric vertical electric fields, *J. Atmos. Terr. Phys.*, Vol. 52, pp. 695 – 705, 1990.

[8] Zadorozhny, A. M., and A. A. Tyutin, Effects of geomagnetic activity on the mesospheric electric fields, *Ann. Geophysicae*, Vol. 16, pp. 1544 – 1551, 1998.

[9] Martynenko, S. I., V. T. Rozumenko, O. F. Tyrnov, A. H. Manson, and C. E. Meek, Statistical parameters of nonisothermal lower ionospheric plasma in the electrically active mesosphere, *Advances in Space Research*, Vol. 35, 1467 – 1471, 2005 (doi: 10.1016/j.asr.2005.03.041).

[10] Meek, C. E., A. H. Manson, S. I. Martynenko, V. T. Rozumenko, and O. F. Tyrnov, Remote sensing of mesospheric electric fields using MF radars, *J. Atmos. Solar-Terr. Phys.*, Vol. 66, 881 – 890, 2004 (doi: 10.1016/j.jastp.2004.02.002, 2004).

[11] Martynenko, S. I., Statistical properties of large mesospheric electric fields, *J. Atmos. Electricity*, Vol. 22, No. 2, pp. 101 – 106, 2002.

[12] Martynenko, S. I., V. T. Rozumenko, and O. F. Tyrnov, New Possibilities for Mesospheric Electricity Diagnostics, *Adv. Space Res.*, Vol. 27, pp. 1127 – 1132, 2001.

[13] Martynenko, S. I., V. T. Rozumenko, A. M. Tsymbal, O. F. Tyrnov, and A. M. Gokov, Mesospheric electric field measurements with a partial reflection radar, *J. Atmos. Electricity*, Vol. 19, pp. 81 – 86, 1999.

[14] Martynenko, S. I., Atmospheric electric field and disturbances of the lower ionosphere parameters, *J. Atmos. Electricity*, Vol. 19, pp. 1 – 9, 1999.

[15] Manson, A.H., C.E. Meek, S.K. Avery, and D. Thorsen, Ionospheric and dynamical characteristics of the mesosphere-lower thermosphere region over Platteville (40ºN, 105ºW) and comparisons with the region over Saskatoon (52ºN, 107ºW), *J. Geophys. Res.*, Vol. 108 No. D13, pp. 4398, doi:10.1029/2002JD002835, 2003.

[16] Gardner, F.F., and J.L. Pawsey, Study of the ionospheric D-region using partial reflections. *J. Atm. Terr. Phys.*, Vol. 3, No. 6, pp. 321–344, 1953.

[17] Tyrnov, O. F., K. P. Garmash, A. M. Gokov, A. I. Gritchin, V. L. Dorohov, L. G. Kontzevaya, L. S. Kostrov, S. G. Leus, S. I. Martynenko, V. A. Misyura, V. A. Podnos, S. N. Pokhilko, V. T. Rozumenko, V. G. Somov, A. M. Tsymbal, L. F. Chernogor, A. S. Shemet, The Radiophysical Observatory for remote sounding of the ionosphere, *Turkish J. of Physics*, Vol. 18, No. 11, pp. 1260 – 1265, 1994.

[18] Belrose, J. S., and M. J. Burke, A study of the lower ionosphere using partial reflections. 1. Experimental technique and method of analysis, *J. Geophys. Res.*, Vol. 69, No. 13, pp. 2799–2818, 1964.

[19] Martynenko, S. I., A Technique for Remotely Sensing Ionospheric Disturbances from Large Mesospheric Electric Fields (in Russian), *Radio Physics and Radio Astronomy*, Vol. 8, No. 2, pp. 127 – 136, 2003.

[20] Gurevich, A. V., Nonlinear Phenomena in the Ionosphere, Springer-Verlag, New York, 1978, X, 370 pp.

[21] Tomko, A. A., A. J. Ferraro, H. S. Lee, A. P. Mitra, A theoretical model of *D*-region ion chemistry modifications during high power radio wave heating, *J. Atmos. Terr. Phys.*, Vol. 42, No. 3, pp.275 – 285, 1980.

[22] Gokov, A. M., and S. I. Martynenko, Changes in the electron collision frequency and electric field in the lower ionosphere (in Russian), *Geomagnetism and Aeronomy*, Vol. 37, No. 2, pp. 76 – 80, 1997.

[23] Hudson, D. J., *Statistics*, Geneva, 1964.

[24] McEwan, M. J., L. F. Phillips, *Chemistry of the Atmosphere*, Edward Arnold, New Zealand, 1975.

[25] Krinberg, I. A., V. I. Vyborov, V. V. Koshelev, V. V. Popov, N. A. Sutyrin, *Adaptive Ionospheric Model* (in Russian), Science, Moscow, 1986, 132 pp.

[26] Schunk, R. W., A. F. Nagy, *Ionospheres — Physics, Plasma Physics, and Chemistry*, Cambridge University Press, Cambridge, 2000.

[27] Larsen, M. F., Frequent and persistent unstable layers in the mesosphere and lower thermosphere, *The CEDAR Post*, vol. 41, pp. 13 – 15, January 2001.

[28] Massey, H., *Negative Ions*, Cambridge University Press, Cambridge, 3rd. ed., 1976.

[29] Ingels, J., D. Nevejans, P. Frederick, E. Arijs, Stratospheric positive ion composition measurements between 22 and 45 km – an updated analysis, *Aeron. Acta.*, Vol. A, No. 304, pp. 1 – 23, 1986.

[30] Dorman, L. I., I. D. Kozin, *Cosmic Radiation in the Upper Atmosphere* (in Russian), Science, Moscow, 1983, 151 p..

[31] Volland, H., *Atmospheric Electrodynamics*, Springer-Verlag, Berlin, 1984.

[32] Vincent, R. A., Planetary and gravity waves in the mesosphere and lower thermosphere, *Adv. Space Res.*, Vol. 7, No. 10, pp. (10)163 – (10)169, 1987.

[33] Bragin, Yu. A., A. A. Tyutin, A. A. Kocheev, A. A. Tyutin, Direct measurement of the atmospheric vertical electric field intensity up to 80 km (in Russian), *Cosmic Res.*, Vol. 12, No. 2, pp. 306 – 308, 1974.

[34] Richard L. Collins, *CEDAR Lidar Beyond Phase III; Accomplishments, Requirements and Goals*, Geophysical Institute, University of Alaska Fairbanks, March 2004, rlc@gi.alaska.edu http://cedarweb.hao.ucar.edu/docs/CLRV1.pdf http://cedarweb.hao.ucar.edu/docs/CLRV2.pdf.

[35] Roussel-Dupre, R., and A. V. Gurevich, On runaway breakdown and upward propagating discharges, *J. Geophys. Res.*, Vol. 101, No A2, pp. 2297 – 2311, 1996.

[36] Davies, K., *Ionospheric Radio*. London, Peter Peregrinus Ltd., 1990.

[37] Fuks, I. M., R. S. Shubova, and S. I. Martynenko, Lower ionosphere response to conductivity variations of the near-earth atmosphere, *J. Atmos. Solar-Terr. Phys*., Vol. 59, 961, 1997.

[38] Bass, F. G., and I. M. Fuks, *Wave Scattering from Statistically Rough Surfaces*. Oxford, Pergamon Press, Ltd. (International Series in Natural Philosophy. Volume 93), 1979.

VLF Phase Perturbations Produced by the Variability in Large (V/m) Mesospheric Electric Fields in the 60 – 70 km Altitude Range

A.H. Manson, C.E. Meek, S.I. Martynenko,
V.T. Rozumenko, O.F. Tyrnov

Canada & Ukraine

Overview

- Historical review
- Remote sensing technique for electric field measurements
- Disturbances in conductivity profiles
- VLF phase perturbations
- Clustered instrument studies
- Conclusions

Historical Review

First Measurements

1974

Rocket-borne field mill.

Yu. A. Bragin, A.A. Tyutin, A.A. Kocheev, and A.A. Tyutin, Direct measurement of the atmospheric vertical electric field intensity up to 80 km. *Cosmic Res., 12.* 279, 1974.

Historical Review

Rocket Electric Field Data

N.C. Maynard, L.C. Hale, J.D. Mitchell, F.J. Schmidlin, R.A. Goldberg, J.R. Barcus, F. Soraas, and C.L. Croskey, Electrical structure in the high latitude middle atmosphere, *J. Atmos. Terr. Phys., 46, №1,* 1984.

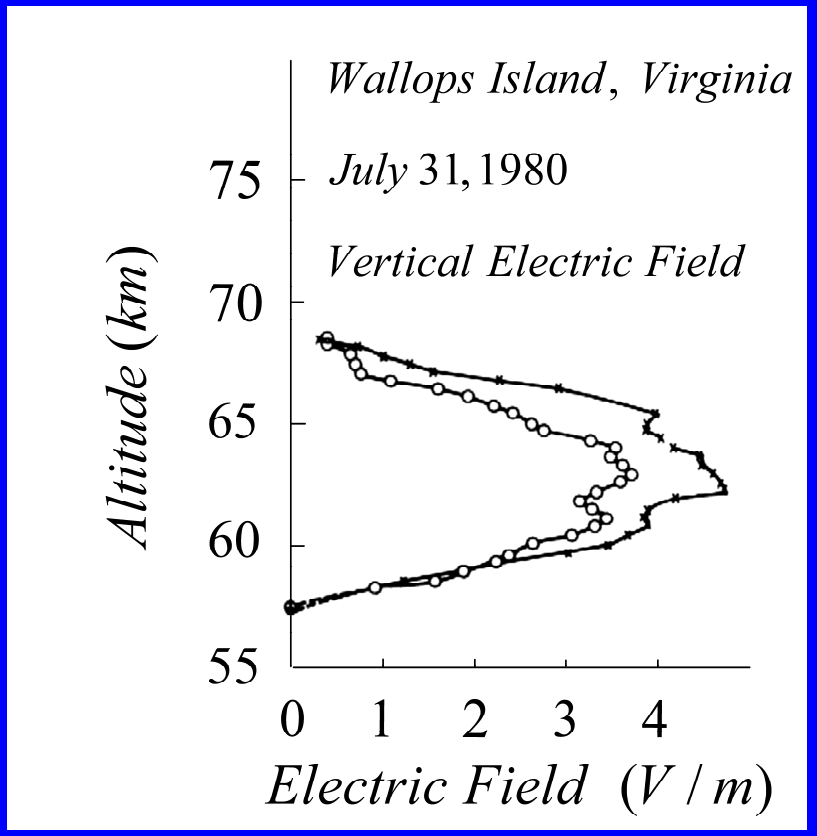

Historical Review

Worldwide Rocket Database

- 1974 – 2006
- Less than 100 rockets launches

Conclusion

- Not enough launch data to address VLF phase perturbations
- To achieve a breakthrough, a remote sensing technique employing radio waves is required

Remote Sensing Technique

Instrumentation

MF Radar:

- 2.2 MHz operating frequency
- 20-μs pulse
- 300 × 300 m^2 transmitter antenna
- Receiving array of two circularly polarized antennas

Remote Sensing Technique

Data Acquired

Magnetoionic Components:

- Amplitudes of **right-handed** circularly polarized waves
- Amplitudes of **left-handed** circularly polarized waves
- **Backscattered from 60- to 70-km altitude**

Remote Sensing Technique Data Input

- The input data for our MF radar technique consists of the ratios of the sample ordinary and extraordinary amplitudes squared
- Backscattered from 60- to 70-km altitude

Remote Sensing Technique

MF Radars Used at Present

Measured vs. **Required Features**

- Signal-to-noise ratio regularly falls below the acceptable level
  - **Temporal continuity**
- One-dimensional distribution
  - **3D distribution**

Remote Sensing Technique

Governing Relations

Weakly Ionized Plasma:

Electrons, positive and negative ions, neutrals

- Electron and ion continuity equations
- Energy equation
- Ohm's law for electric fields

Remote Sensing Technique

Basic Relation Derived

- We have related these ratios to the electric field intensity via the electron collision frequency
- We have obtained the following relation for the electric field intensity:

$$E^2 = \frac{km\delta_0 T_{e0}(z_1)}{0.97e^2}\nu_e^2(z_1)\left\{1-\left(\frac{\nu_{e0}(z_1)}{\nu_e(z_1)}\right)^{6/5}\right\}$$

Remote Sensing Technique
Electron Collision Frequency

- First, we apply the "Differential Absorption" technique of **[Belrose, J. S., and M. J. Burke, A study of the lower ionosphere using partial reflections. 1. Experimental technique and method of analysis, *J. Geophys. Res.*, Vol. 69, No. 13, pp. 2799–2818, 1964]** at altitudes of 60 to 70 km and determine the electron collision frequencies

Remote Sensing Technique

MF Radar Electric Field Database

- Canada, **1979 – 1982**

  170 measurements, **10 min** duration
- Ukraine, **1978 – 1994**

  185 measurements, **5 – 10 min** duration

Total MF radar database of
355 measurements

Remote Sensing Technique

MF Radar Measurements

Temporal Variability

- The database consists of separate intervals of measurements collected over the years, therefore the temporal variability they provide is not continuous
- Nevertheless, brief snapshots can be provided

Remote Sensing Technique

MF Radar Measurements

Temporal Variability

- The variability of large mesospheric electric fields displays a wide range of time scales, from an order of one minute (as shown in this figure) to …

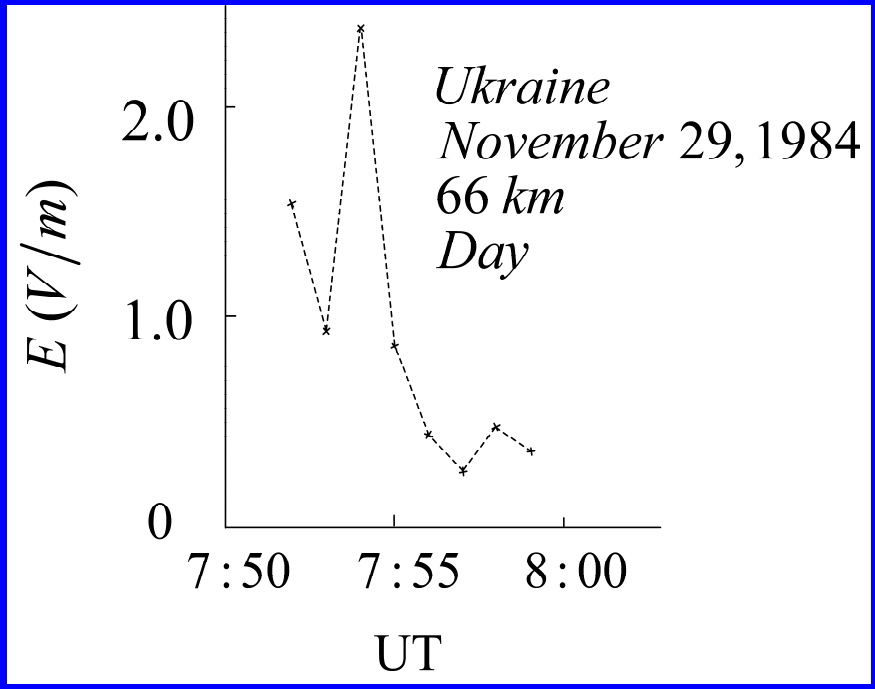

Remote Sensing Technique

MF Radar Measurements

Temporal Variability

- … an order of an hour (as shown in this figure)

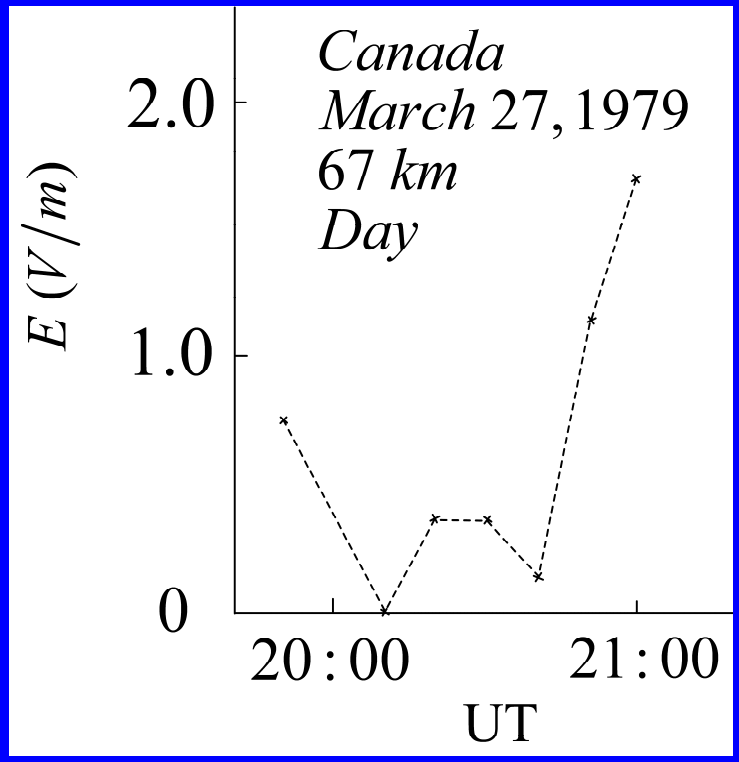

Remote Sensing Technique

MF Radar Measurements

Distribution of Electric Field Intensities

Two parts:

- the main body of
  $0 < E \leq 2.5$ V/m
  ($n = 99$)
- the 'tail' $E > 2.5$ V/m
  ($n = 21$)

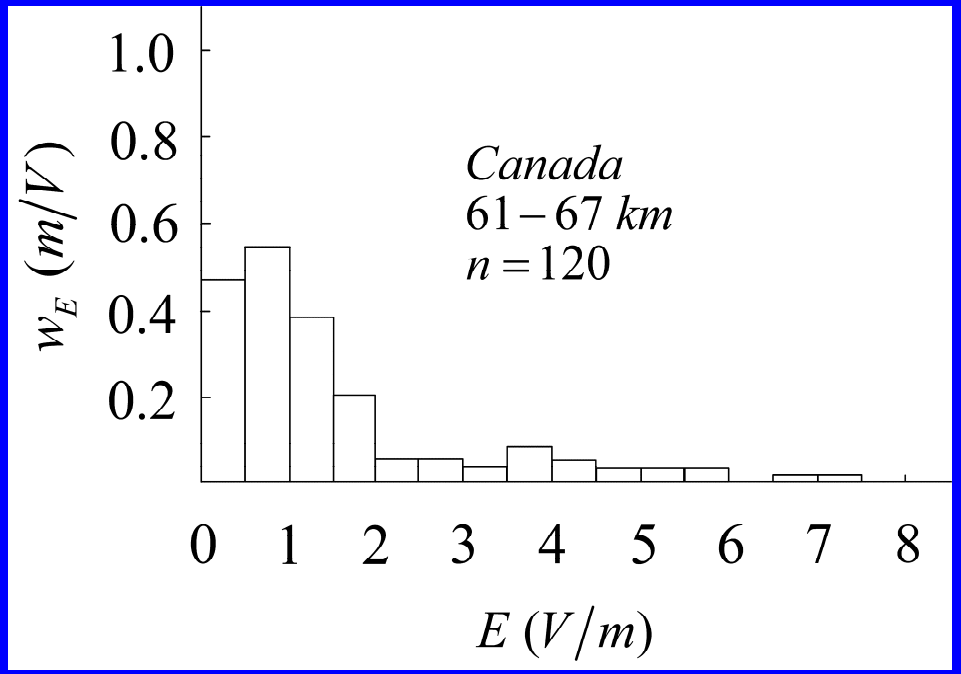

Remote Sensing Technique

MF Radar Measurements

Distribution of Electric Field Intensities

Two parts:

- the main body of
  $0 < E \leq 2.5$ V/m
  ($n = 129$)
- the 'tail' $E > 2.5$ V/m
  ($n = 10$)

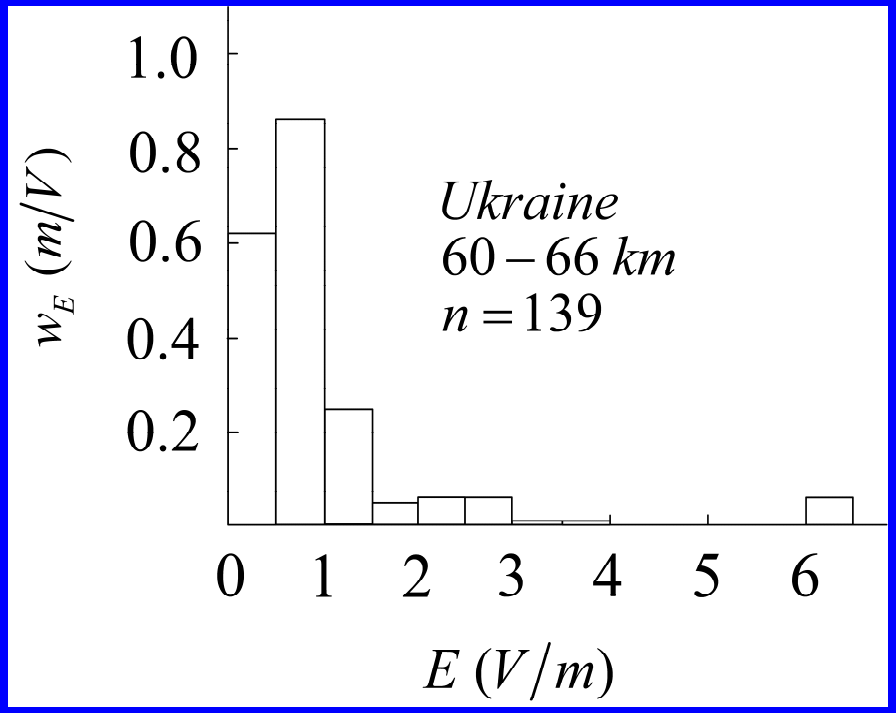

Remote Sensing Technique

MF Radar Measurements

Distribution of Electric Field Intensities

- The main body corresponds to a one-parameter Rayleigh probability density functions as given by

$$f(E) = \frac{E}{\sigma^2} e^{-\frac{E^2}{2\sigma^2}}$$

Disturbances in Conductivity
Electric Field Model

- To model disturbances in conductivity profiles produced by **$0 < E \leq 2.5$ V/m** fields, we have chosen the profile depicted in this figure

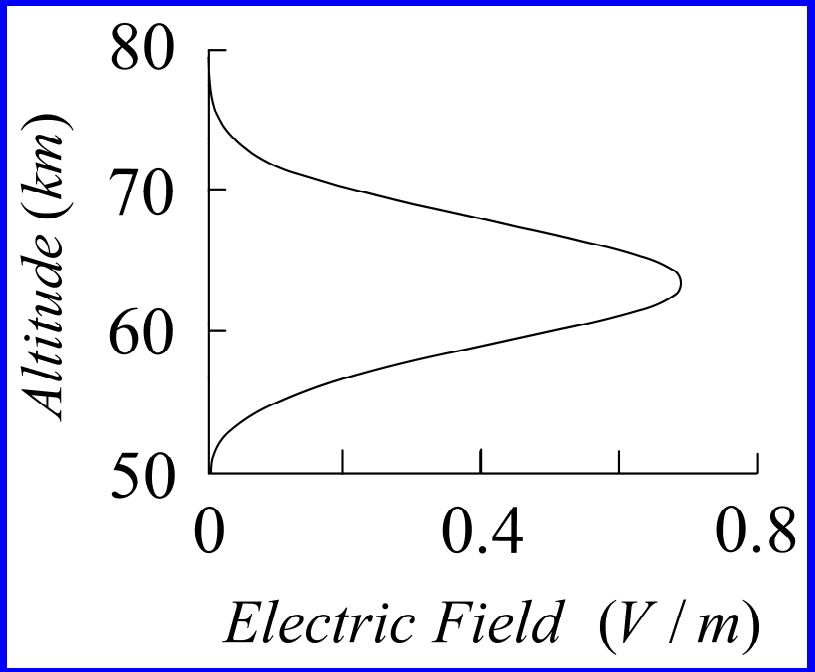

Disturbances in Conductivity
(Daytime Conditions)

- Shown here is the profile of the low-frequency conductivity disturbed (solid line) by the **less than 1 V/m** electric fields and the undisturbed (dashed line) conductivity profile

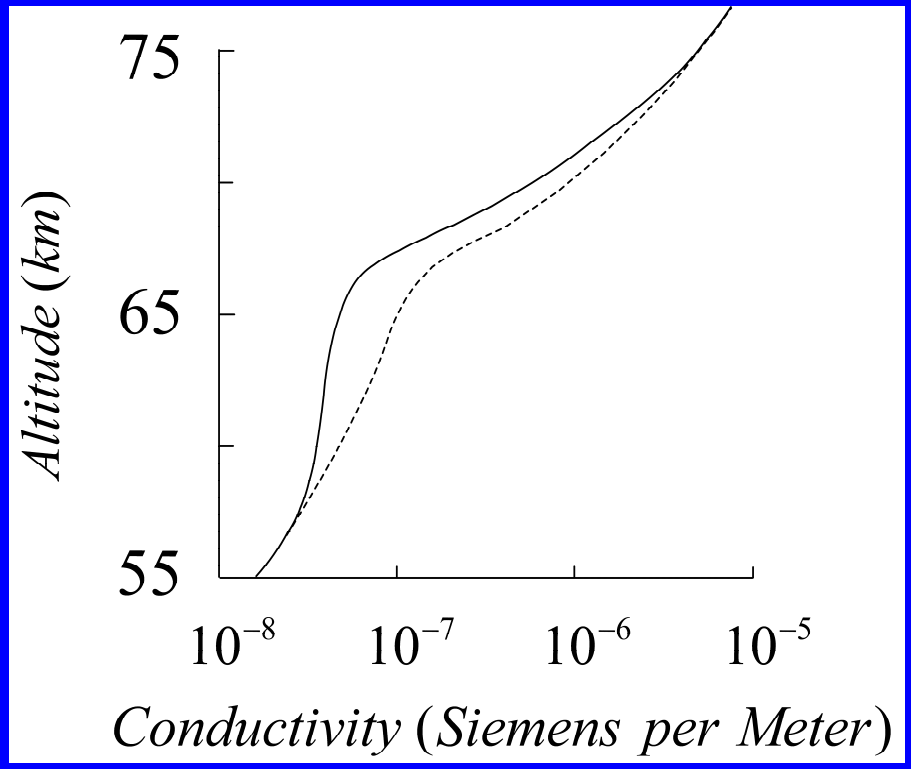

Disturbances in Conductivity
(Nighttime Conditions)

- Shown here is the profile of the low-frequency conductivity disturbed (solid line) by the **less than 1 V/m** electric fields and the undisturbed (dashed line) conductivity profile

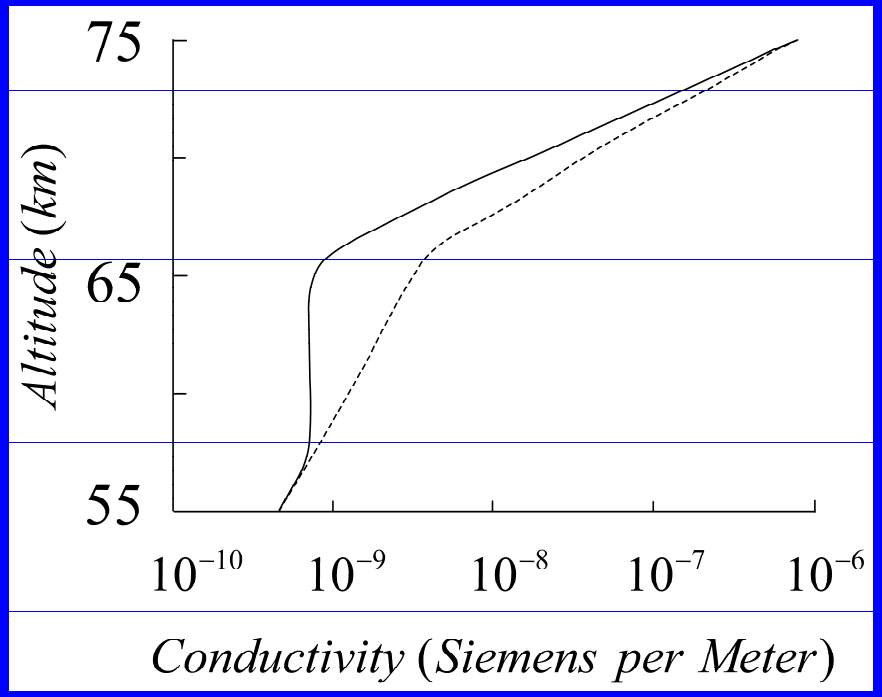

Disturbances in Conductivity
Conclusion

- The electric field variability in the main body of the **$0 < E \leq 2.5$ V/m** distribution leads to variations in the ionospheric conduction contours of up to a few kilometers in altitude

Disturbances in Conductivity
Electric Field Model

- To model disturbances in conductivity profiles produced by ***E* > 2.5 V/m** fields, we have chosen the mean of the profiles depicted in this figure

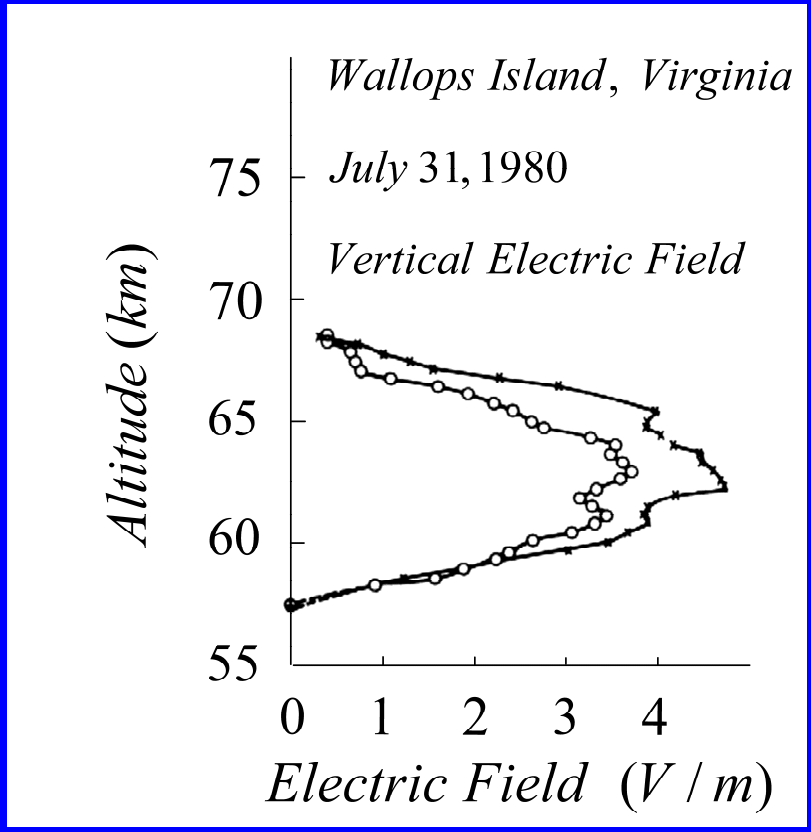

Disturbances in Conductivity
(Daytime Conditions)

- Shown here is the profile of the low-frequency conductivity disturbed (solid line) by the ***E* > 2.5 V/m** electric fields shown in the preceding figure and the undisturbed (dashed line) conductivity profile.

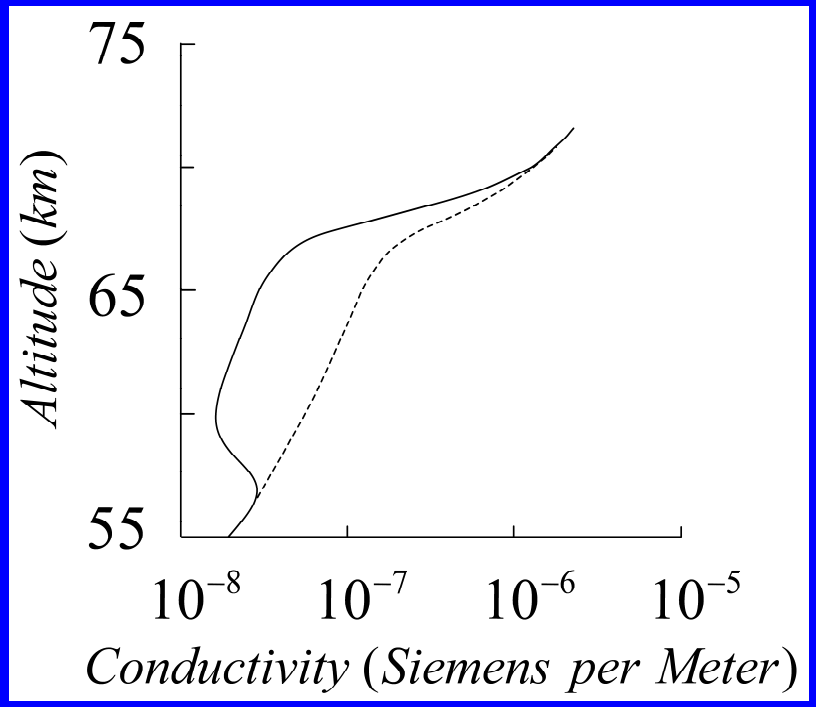

Disturbances in Conductivity
(Nighttime Conditions)

- Shown here is the profile of the low-frequency conductivity disturbed (solid line) by the ***E* > 2.5 V/m** electric fields and the undisturbed (dashed line) conductivity profile

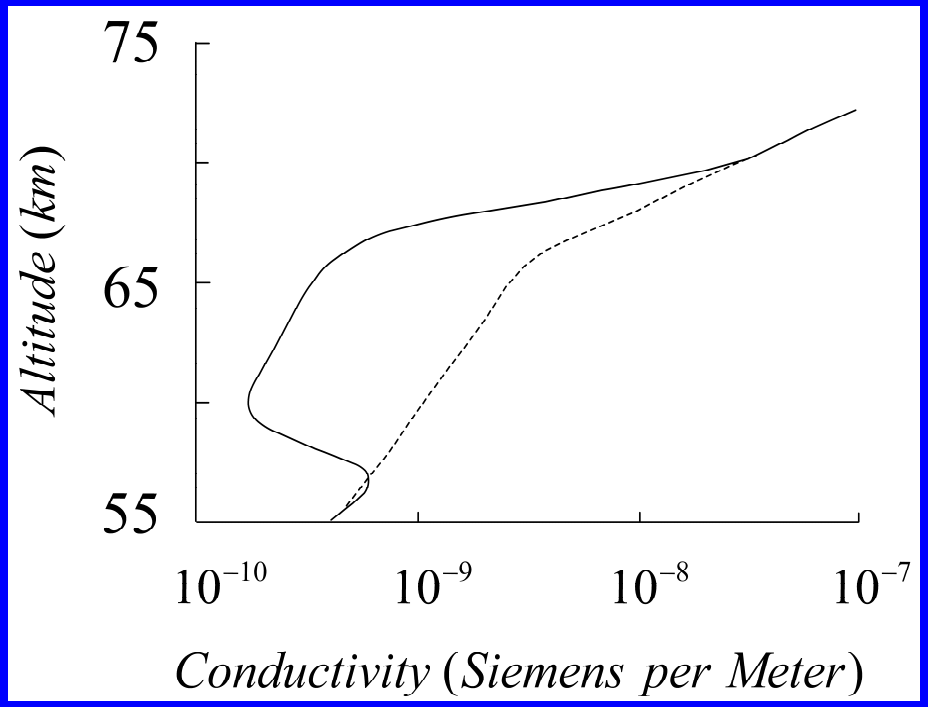

Disturbances in Conductivity

Iso-Conduction Contours

Conclusions

- The disappearance or appearance of electric fields in the main body of their distribution (with a peak of 1 V/m) results in a variation in the height of the ionospheric iso-conduction contours of up to 6 kms in altitude
- The disappearance or appearance of electric fields in the “tail” of their distribution, with a peak of 4 V/m, results in a variation in the height of the ionospheric iso-conduction contours of up to 10 kms in altitude

VLF Phase Perturbations
(Smooth Reflective Surface)

- If the reflective surface were smooth, the VLF phase perturbations would be assessed correctly. The corresponding phase change $\Delta\phi$ over long distances can be given (in radians) by the well-known relation

$$\Delta\phi = -\frac{2\pi d}{\lambda}\left(\frac{h}{2a} + \frac{\lambda^2}{16h^2}\right)\frac{\Delta h}{h}$$

VLF Phase Perturbations
(Smooth Reflective Surface)

- Given this way of thinking, we have attributed the VLF phase variations (at 16 kHz) to variations in the electric fields during the escape of radioactive materials **[I.M. Fuks, R.S. Shubova, and S.I. Martynenko, Lower ionosphere response to conductivity variations of the near-earth atmosphere, *J. Atmos. Solar-Terr. Phys*., Vol. 59, 961, 1997]**

VLF Phase Perturbations
(Rough Reflective Surface)

- The theory of wave scattering requires information on the correlation functions of the deviations of the reflective surface from a smooth surface
- Consequently, the challenge for VLF phase investigations will be to characterize three-dimensional variations in the electric fields intrinsic to the mesosphere

VLF Phase Perturbations
(Rough Reflective Surface)

Engineering Solutions

- A new radar capable of performing elevation and azimuth scans (too complicated!)
- A few relocatable MF radars (ones developed, produced and used by Kharkiv V. Karazin National University)

Clustered Instrument Studies

- One-hop VLF circuits with an MF radar below the region where the ray is reflected may yield new advances in VLF phase perturbation research

Conclusions

- The mesospheric electric fields act to produce local height variations in the ionospheric conduction contours of the order of a few kilometers
- A major breakthrough in this area has been the development of the MF radar technique for sensing electric fields remotely

Conclusions

- The MF radars used so far have low levels of the signal-to-noise ratios, which need to be increased
- The existing MF radars provide only one-dimensional distribution of the electric fields. Thus, the most important challenge for the future will be to develop an MF radar facility capable of determining a 3-dimensional distribution of scattered signals in the MF frequency band

Conclusions

- One-hop VLF circuits with an MF radar below the region where the ray is reflected may yield new advances in VLF phase perturbation research and provide useful information for practical applications